https://doi.org/10.5194/essd-2026-644
Preprint. Discussion started: 26 August 2026

Open Access Earth System Science Data Discussions

Global and systematic stratospheric aerosol number and size distributions from the NOAA Balloon Baseline Stratospheric Aerosol Profiles (B2SAP) project

Kate Smith[1,2], Alexandre Baron[1,2], Joshua Schwarz[2], Elizabeth Asher[1,3], Emrys Hall[3], Patrick Cullis[3], Alex Fritz[1,3], Hagen Telg[1,3], Ross Burgener[4], Bryan Thomas[4], Matthew Martinsen[5], David Nardini[5], Darryl Kuniyuki[5], Penny Smale[6], Ben Liley[6], Richard Querel[6], Krystian Kopka[7], Ian Crocker[1,3,7], Skyler Jordan[7], Michael Doneghey[7], Luke Longren[1,7], Stephanie Evan[8,9], Jerome Brioude[8,9], Jean-Marc Metzger[9], David Combemale[8,9], Cor Becker[10], Dwight Samuel[10], Cheryll Tjon A Ten[10], Mohammed Amierali[10], Christopher Wongsowidjojo[10], Dennis Rodrigues[10], George Paiman[10], Ankie Piters[11], Katrin Müller[12], and Troy Thornberry[2]

[1]Cooperative Institute for Research in Environmental Sciences, University of Colorado, Boulder, CO, USA
[2]NOAA Chemical Sciences Laboratory, 325 Broadway, Boulder, CO, 80305 USA
[3]NOAA Global Monitoring Laboratory, 325 Broadway, Boulder, CO, 80305, USA
[4]NOAA GML Barrow Observatory, Utqiagvik, AK, 99723 USA
[5]NOAA GML Mauna Loa Observatory, Hilo, HI 96720 USA
[6]Earth Sciences New Zealand, 3513 Becks-Lauder Road, Lauder, New Zealand
[7]NOAA GML South Pole Observatory, Amundsen-Scott South Pole Station, Antarctica
[8]Laboratoire de l'Atmosphère et des Cyclones (LACy), Université de la Réunion, Saint-Denis, France
[9]Observatoire des Sciences de l'Univers de la Réunion, Université de la Réunion, Saint-Denis, France
[10]Meteorological Service of Suriname (MDS), Paramaribo, Suriname
[11]Royal Netherlands Meteorological Institute (KNMI), De Bilt, The Netherlands
[12]Alfred Wegener Institute (AWI), Helmholtz Centre for Polar and Marine Research, Potsdam, Germany

Correspondence: Kate Smith (katie.smith@noaa.gov)

Abstract. Stratospheric aerosol plays critical roles in the global radiative balance and stratospheric chemistry. A robust evaluation of stratospheric aerosol abundance and size distributions over time is required to determine and accurately model aerosol impacts on the Earth system. The Balloon Baseline Stratospheric Aerosol Profiles (B^2SAP) project uses weather balloons to collect regular vertical profiles of stratospheric aerosol number and size distributions, at eight latitudinally diverse locations across the globe from the ground to ~30 km altitude. These systematic *in situ* measurements allow the micro-physical properties of the background stratospheric aerosol and their variability to be examined. These on-going measurements provide constraints for aerosol modules of large coupled models and reference for satellite retrievals relying on previous size distribution assumptions. The lightweight, low-powered Portable Optical Particle Spectrometer (POPS) instrument is deployed on balloon platforms, allowing for high vertical resolution and the detection of stratospheric aerosol down to 140 nm diameter. This paper presents the B^2SAP aerosol dataset (DOI: https://doi.org/10.25921/mchy-y552, (Smith et al., 2026)), including a description of the B^2SAP network, POPS measurement principles, sensitivity analysis, calibration procedures, file processing workflow and a comparison with aerosol extinction from the GloSSAC product.

https://doi.org/10.5194/essd-2026-644
Preprint. Discussion started: 26 August 2026

Open Access Earth System Science Data Discussions

1 Introduction

Stratospheric aerosol plays a key role in the global radiation budget as incoming solar radiation is scattered and absorbed by stratospheric aerosol (SA), affecting the amount of radiation reaching the Earth's surface (Solomon et al., 2011; Murphy, 2009). Direct incoming solar radiation in the visible wavelengths interacts with SA, and roughly a quarter of the scattered light is returned to outer space, while the other fraction is scattered forward, becoming diffuse sunlight (Murphy, 2009). The greater the concentration of stratospheric aerosol, and the larger the optical particle diameter, the more efficient the aerosol becomes at scattering and absorbing light (Murphy et al., 2021), leading to a larger contribution to solar radiation extinction and hence surface cooling (McCormick et al., 1995; Wrana et al., 2021). Stratospheric aerosol also has significant implications for heterogeneous chemistry, as chemical reactions are facilitated by aerosol surfaces, the most notorious of these being halogen activation, which causes the depletion of stratospheric ozone (Hazra et al., 2019; Lawler et al., 2025; Solomon et al., 1986; Wegner et al., 2012).

Previous measurements have shown that stratospheric aerosol is predominantly composed of a mixture of sulfuric acid and water (Junge and Manson, 1961; Murphy et al., 2021). SA is primarily formed by sulfur containing tropospheric source gases (the main two being sulfur dioxide (SO_2) and carbonyl sulfide (OCS)) becoming oxidized to gaseous sulfuric acid after entering the stratosphere (Turco et al., 1982). Gaseous sulfuric acid rapidly condenses and nucleates with water vapor to result in aqueous sulfuric acid, referred to here as sulfate aerosol (Brodowsky et al., 2024). A combination of gravitational settling and evaporation of aerosol associated with increasing stratospheric temperatures at higher altitudes constrain the majority of SA to a region between the tropopause and approximately 30 km altitude (Murphy, 2009). The global, persistent layer of SA was first observed using high altitude balloon platforms (Junge et al., 1961) and is referred to as the stratospheric aerosol layer or Junge Layer (Bigg et al., 1970; Junge and Manson, 1961). Previous observations of the background lower stratosphere indicate the aerosol diameter can range between 100 – 2000 nm (Bigg et al., 1970; Thomason and Burton, 2008) with the majority of aerosol exhibiting optical diameters at the smaller end of this range. Typically the size distribution is bimodal, with modes centered around 200 nm and 400 - 700 nm diameter (Murphy et al., 2021; Lawler et al., 2025). The smaller mode generally contains mixed organic sulfur tropospheric aerosols that have been transported across the tropopause (Murphy et al., 2021) and this mode shifts to smaller diameters for air masses with either very recent tropospheric input or aged air masses with a lower N_2O concentration (Lyu et al., 2026).

Balloons are a proven method for making stratospheric aerosol observations. There is a long record of optical particle counters (OPCs) integrated onto a balloon platform to study trends in stratospheric aerosol size distributions for particles with an optical diameter of greater than 0.3 μm from 1971 - present day from Laramie, Wyoming (Kalnajs and Deshler, 2022). Monthly stratospheric size distributions from OPCs on the balloon platform were used to assess long-term aerosol trends within this northern mid-latitude band, and evaluate stratospheric background and impact upon SA following volcanic eruptions (Jäger and Deshler, 2002). This 50+ year record serves as a powerful tool for the validation of remote sensing

https://doi.org/10.5194/essd-2026-644
Preprint. Discussion started: 26 August 2026

techniques for stratospheric aerosol. This dataset validated profiles of SA extinction from SAM, SAGE-II, HALOE (Hervig and Deshler, 2002), CLAES, ISAMS, and SAGE-III (Kalnajs and Deshler, 2022), as well as being used to interpret and expand upon mid-latitude lidar backscatter measurements (Deshler et al., 2006). The B^{2}SAP network aims to complement and expand upon this exemplary record by having multiple launch locations within different latitude bands to build up a picture of global SA abundance and variability. The POPS instrument capable of optically sizing sulfate particles down to 140 nm diameter (Gao et al., 2016), a huge strength enabling B^{2}SAP to capture more of the smaller sized particles. Obtaining quarterly *in situ* aerosol size distribution profiles within a global network will allow the spatiotemporal variability of SA size distributions to be investigated. Aircraft have also been used to make *in situ* observations of stratospheric aerosol during field missions such as ACCLIP (Ueyama et al., 2025; Zhu et al., 2024), DCOTTS (Li et al., 2021, 2023) and SABRE (Gurganus et al., 2026; Lawler et al., 2025). This is useful for providing a highly resolved snapshot of the properties of stratospheric aerosol, but aircraft-based observations are limited by a ceiling of 21 km altitude, and hence aircraft measurements reflect the lower stratosphere, and may only partially penetrate the Junge Layer. The expense of using aircraft for stratospheric aerosol observations prohibits systematic observations at multiple locations, making global stratospheric aerosol analysis and trend estimations scientifically challenging. Aircraft missions require a lot of planning and financial resources, limiting their capacity for rapidly responding to unpredictable stratospheric perturbations i.e. from explosive volcanoes. The B^{2}SAP payload aims to fill the gap between these intensive aircraft missions, with a low-cost, portable method that reaches 30 km and is reproducible for regular launches occurring globally, all year round. The B^{2}SAP fast deployment, in response to the Hunga-Tonga eruption was demonstrated in (Asher et al., 2023), where balloons were launched 7 and 10 days after the volcanic eruption. This response, enabling the early study of the volcanic plume yielded a unique set of observations that were able to detect 'unexpected rapid aerosol formation' would be difficult to accomplish with aircraft.

The stratosphere is frequently perturbed by large-scale events, such as explosive volcanic eruptions (Asher et al., 2023; Eckhardt et al., 2008), dust plumes (Li et al., 2025) or extreme wildfires (Ohneiser et al., 2022) leading to a "persistently variable" (Solomon et al., 2011) stratospheric aerosol background, making it difficult to even identify quiescent periods (Robock, 2000). Observations of enhanced SA loading, with associated increases in both aerosol abundance and size, led to enhanced albedo effects resulting in measurable surface cooling impacts that can persist for several years. The 1991 Mt. Pinatubo eruption led to an aerosol mass loading of 30 Tg (McCormick et al., 1995) into the stratosphere which resulted in 0.5-0.8 ^{o}C of global surface cooling for 18 months after the initial eruption (Robock, 2000; Minnis et al., 1993). Global stratospheric dynamics were influenced by the newly nucleated aerosol as these aerosol absorbed outgoing long-wave radiation, inducing local warming in the lower tropical stratosphere, resulting in enhanced lofting at the tropics and accelerated horizontal transport of air masses (McCormick et al., 1995). There is an increasing frequency of occurrence of stratospheric smoke plumes from large wildfires, with an associated increase in particle extinction coefficients and notable reduction in ozone from the activation of reactive halogen species on a hemispheric scale (Ohneiser et al., 2022; Solomon et al., 2023).

Several studies have performed SA trend analyses with differing conclusions; (Deshler et al., 2006) stated that, between 1970 – 2004 there was no significant trend in the background stratospheric aerosol number concentrations, whereas (Hofmann et al., 2009) concluded that a positive trend increase in stratospheric aerosol abundance since 2002 was associated with an

https://doi.org/10.5194/essd-2026-644
Preprint. Discussion started: 26 August 2026

increase in SO_2 emissions lofted by convection within the Asian Summer Monsoon. Other studies, (Vernier et al., 2011; Trickl et al., 2013) argue that increases in stratospheric aerosol concentrations are likely due to moderate volcanic eruptions (Volcanic Explosivity Index = 4). Aerosols can be directly injected to the stratosphere, or indirectly, through aerosol-forming gases such as SO_2 or H_2S (Robock, 2000). The degree to which stratospheric aerosol disturbances impact the global radiative budget is highly dependent upon the amount of injected material, the injection altitude and the size of the resulting aerosols. The extent to which aerosol size distribution changes after stratospheric perturbation events is not well understood, which is crucial for calculating the changes to the radiative balance from such events (Wrana et al., 2021). Large uncertainties remain regarding the abundance and variability of these stratospheric particles (Von Savigny and Hoffmann, 2020). This is partly due to the challenging nature of obtaining measurements in the stratosphere's remote environment associated with cold temperatures, low pressures and high altitudes. The uncertainty associated with understanding the stratospheric aerosol layer leads to low confidence when predicting the climate with global circulation models (Stenchikov et al., 2006; Regayre et al., 2026) and forecasting climate change. Evaluating the background abundance and variability of stratospheric aerosol is imperative for understanding and accurately quantifying changes to stratospheric aerosol. Linking the magnitude of stratospheric perturbations to changes in aerosol size distributions is essential for accurately predicting the radiative, chemical and dynamical impacts of these perturbations. We present the technical aspects of the Balloon Baseline Stratospheric Aerosol Profiles (B^2SAP) effort and outline available data from the Portable Optical Particle Spectrometer (POPS, Handix Inc, Boulder, CO, USA) used to accurately measure stratospheric aerosol number and size distributions at high vertical resolution. These *in situ* observations allow for the direct parameterization of micro-physical processes which improves the representation of stratospheric aerosol properties. This reduces the uncertainty in estimating the global radiative transfer calculations and increases our knowledge of stratospheric chemical mechanisms, providing reliable inputs for stratospheric modeling. High vertical resolution measurements provide the capacity to constrain stratospheric aerosol plumes, enabling the detection of the plume edges and allowing for source apportionment via backward trajectories. Regular B^2SAP launches are imperative for understanding both background short term variability and multi-year trends. Better constraining the SA size distribution temporal variability will lead to higher confidence in the identification and quantification of stratospheric perturbations. As solar radiation management techniques - such as stratospheric aerosol injection (SAI) - become increasingly considered, this dataset provides invaluable baseline information on the background state and natural variability of stratospheric aerosol. This work will provide an overview of the B^2SAP project, followed by a description of instrumentation used to measure aerosol size distributions, including calibration and sensitivity studies. Lastly, we have performed some analyses with this dataset and comparisons with remote sensing techniques.

2 The B^2SAP project

The dataset presented here was collected by a series of balloon launches occurring on a regular basis to collect direct aerosol size distribution measurements. Launches are on-going and date back to 2019 for some sites. The B^2SAP project is one portion

https://doi.org/10.5194/essd-2026-644
Preprint. Discussion started: 26 August 2026

of NOAAs Earth Radiation Budget (ERB, https://csl.noaa.gov/research/erb/) program, funded to improve our understanding of the stratosphere and its contribution to Earths energy balance.

2.1 Payload and platform

The payload (Figure 1) is the result of a collaboration between two complementary programs - B^{2}SAP and NOAA GML's GLobal Ozone and Water vapor (GLO_3W) program. The focus of this study, B^{2}SAP, refers to the data from the Portable Optical Particle Spectrometer (POPS) to measure aerosol size distribution and concentrations. GlO_3W program operates an electrochemical concentration cell, ECC, (Sterling et al., 2018) to measure ozone mixing ratios and a frost point hygrometer, FPH, (Hall et al., 2016) for measurements of water vapor mixing ratio. A full B^{2}SAP+GLO_3 payload consists of a POPS, ECC and FPH. Location (GPS, including altitude) and environmental (pressure, temperature, humidity, wind) data is obtained using an iMet (International Met Systems) radiosonde which telemeters data from the balloon to a ground-based receiving station. A helium-filled latex balloon (Hyowee or Totex, typically 1200g to 1600g) carries the payload to the middle stratosphere, around 30 km altitude. A valve equipped with a pressure sensor is set to open at ~13 mb (28-30 km). Helium slowly leaks out from the balloon, decreasing the buoyancy of the balloon and leading to a steady descent speed that is similar to the rate the balloon ascended (5 m s^{-1}). The B^{2}SAP payload weighs less than 6 lb (2.7 kg) and is thus compliant with the 14 CFR regulation set by the Federal Aviation Administration and Stratospheric Ballooning Association that requires additional constraint and notices required for unmanned balloons with a single payload that weighs more than 6 lbs. This article and the B^{2}SAP dataset focuses specifically on the aerosol concentration and size distribution observations obtained from the Portable Optical Particle Spectrometer (POPS) instrument.

2.2 Geographic Distribution

There are currently 10 launch sites where B^{2}SAP payloads have flown (Fig. 2, Table A1 and A2), strategically chosen to capture background stratospheric aerosol abundance and variability. Large global circulation dynamics cause a lot of latitudinal variability within the background stratosphere. Therefore, the B^{2}SAP program is composed of latitudinally diverse launch sites to build a picture of the global distribution of the stratospheric aerosol layer (Figure 2 and Table A1). Due to strong horizontal mixing the stratosphere is considered relatively homogeneous longitudinally, however due to the availability of resources B^{2}SAP operates from launch sites which also cover a range of longitudes. This will provide additional information regarding the representation of the global stratosphere and allow for stratospheric dynamics and aerosol injection plume tracking to be evaluated. Boulder, Colorado, USA experiences the most frequent launches with a full B^{2}SAP/GlO_3W payload flown every two to three weeks. The other sites are operated by collaborators who receive calibrated instrumentation from the National Oceanic and Atmospheric Administration (NOAA) Boulder laboratories before performing quarterly launches on our behalf. Two of the launch locations, San Pedro (Costa Rica) and Scott Base (Antarctica) operate on an opportunistic basis (Table A2), where launches are not regular but occurred due to personnel traveling as part of a different program, hence these are separated from the more regular locations in Fig. 2 and Table A1. It is well known that there is a lack of stratospheric observations made in the tropics, due in part to the higher tropopause height. This leads to large uncertainties in tropical model representations,

https://doi.org/10.5194/essd-2026-644
Preprint. Discussion started: 26 August 2026

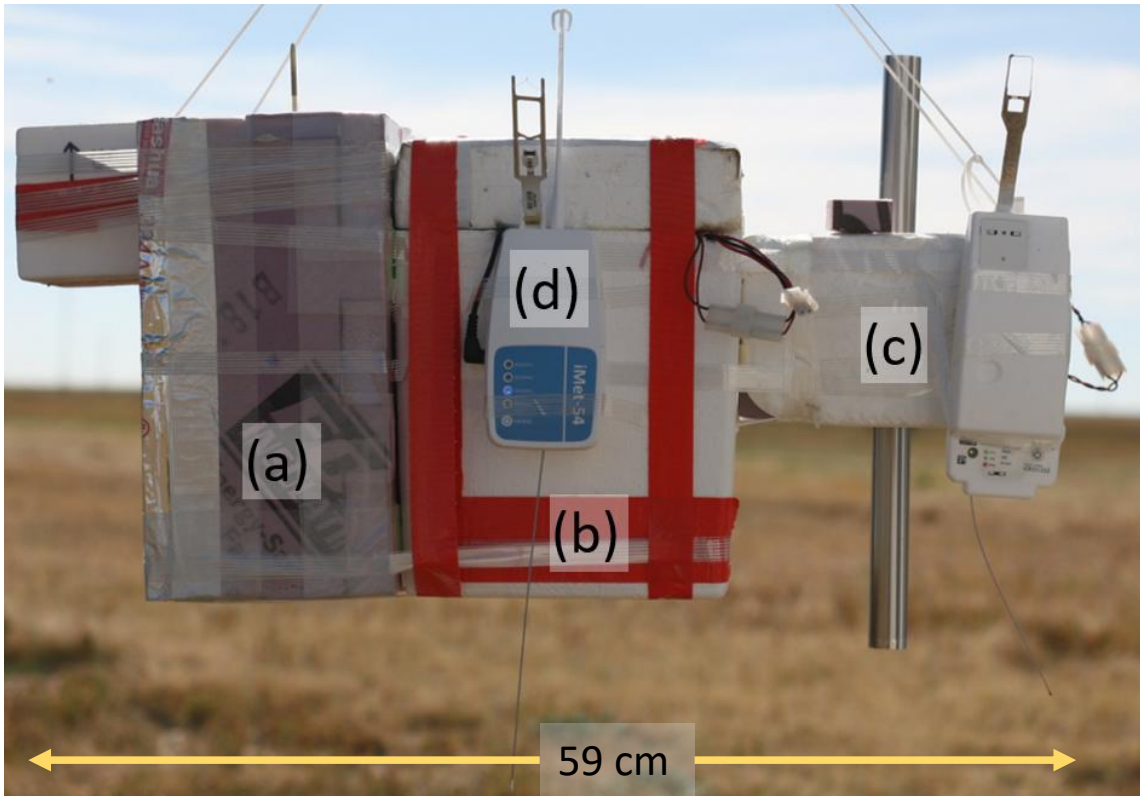

Figure 1. The B^2SAP/GlO_3W payload ready for a launch consists of, a) POPS for aerosol measurements, b) electrochemical concentration cell (ECC) for ozone, (c) frost point hygrometer (FPH) for water vapor, and (d) an iMet-54 radiosonde for data telemetry, as well as location and meteorological variables.

a region of particular interest as it is where the Brewer-Dobson circulation lofts tropospheric material into the stratosphere (Brodowsky et al., 2024). This transport pathway is the main route for sulfur-containing trace gases such as SO_2 and OCS to undergo troposphere-stratosphere exchange and enter the lower stratosphere (18-25 km) (Khaykin et al., 2017). Tropical profiles are essential for understanding the stratospheric aerosol layer in this region of intense convective transport (Pan et al., 2017). From 2025, B^2SAP/GlO_3W payloads have been launched at two tropical locations; Suriname (5.7 ^{o}N) and Palau (7.3 ^{o}N) in an attempt to fill this data gap.

3 Portable Optical Particle Spectrometer (POPS)

The Portable Optical Particle Spectrometer (POPS) is a lightweight (600 g), portable (175 x 162 x 88 mm), low-power (5W) particle counter spectrometer (Gao et al., 2016) that measures aerosol size distributions upon the B^2SAP payload.

https://doi.org/10.5194/essd-2026-644
Preprint. Discussion started: 26 August 2026

Open Access Earth System Science Data Discussions

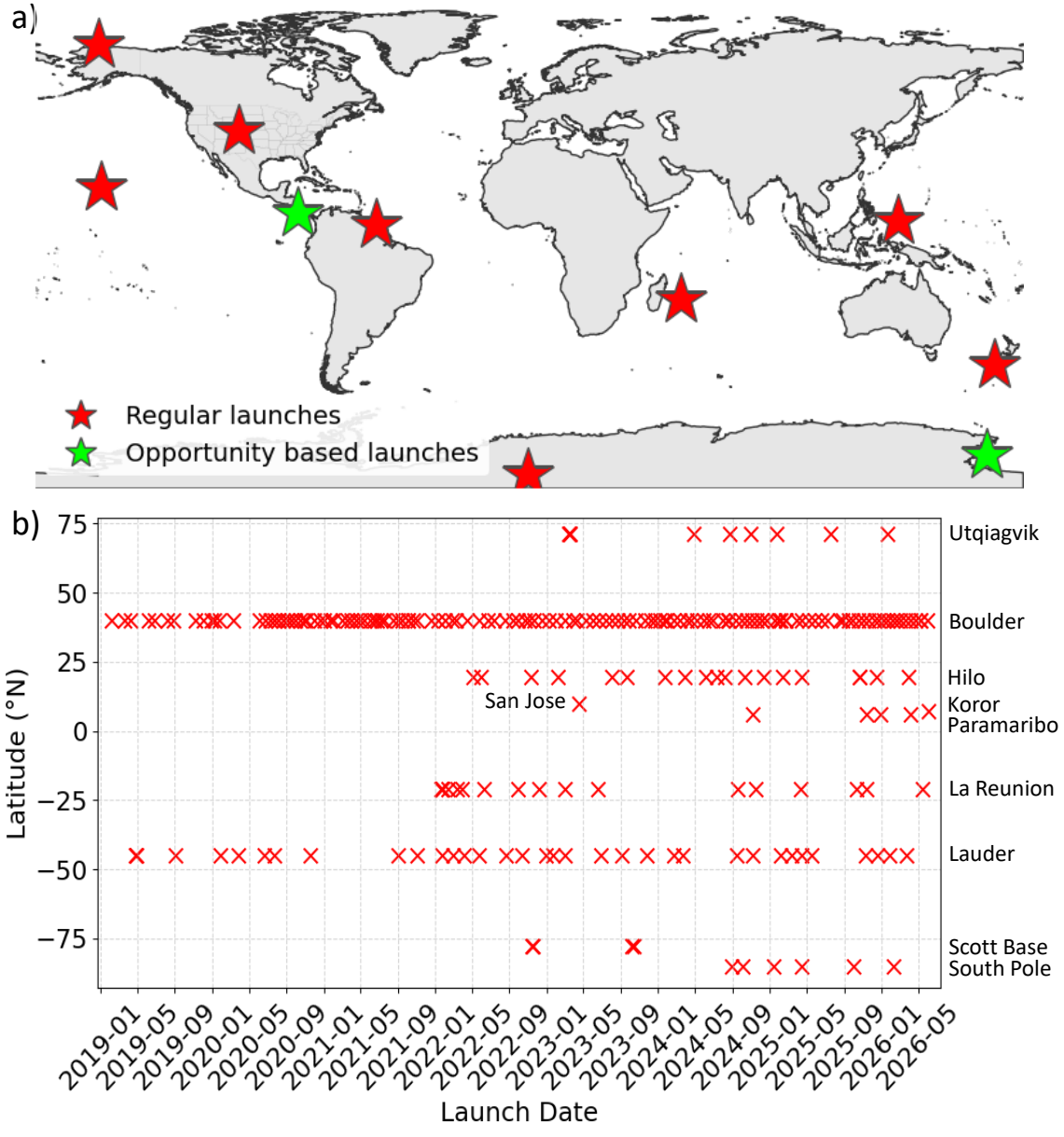

Figure 2. The B^{2}SAP launch sites have been strategically located at a range of latitudes to be globally representative of the stratosphere (a). The stratosphere is relatively uniform across different longitudes but has large variability over latitudes due to stratospheric dynamics. Boulder, CO, USA has the most frequently launched B^{2}SAP payloads, with the other regular (red stars) sites aiming for quarterly balloon observations (b). B^{2}SAP balloon launches have been occurring at the mid-latitude sites since 2019. There are 5 profiles within the B^{2}SAP dataset as a result of opportunity based launches (green stars) from Costa Rica and Scott Base Antarctica.

https://doi.org/10.5194/essd-2026-644
Preprint. Discussion started: 26 August 2026

Open Access Earth System Science Data Discussions

3.1 POPS Particle Detection

The main physical components of the POPS instrument are: a brass inlet to sample the air, a laminar flow element (LFE) to accurately measure the volume of air sampled, an optical chamber containing the laser, a photomultiplier (PMT) to detect scattered light, and a pump to pull air through the optical chamber (Appendix B, Fig. B1). The POPS photomultiplier identifies individual particles moving through the POPS optical chamber and this produces a signal (peak). For POPS to identify a peak as a particle the maximum amplitude of the peak must be three times the standard deviation (3σ) of the POPS baseline, see Section 3.3, Figure 4. Every particle entering the POPS inlet that produces a peak with an amplitude greater than the 3σ threshold will be counted and optically sized by relating the maximum scattering amplitude to an optical diameter using Mie theory (Section 3.2) for an assumed index of refraction (n). The POPS only becomes saturated when there are more than 10,000 particles $\sec^{-1}$ arriving at the inlet. For the stratosphere this criterion is very unlikely to be met. A full description of the design of the POPS can be found in (Gao et al., 2016), and the calibration procedure is included in Section 4.

3.2 Mie Theory

OPCs use the same underlying principle for determining the optical diameter of individual particles from the amount of scattered light they produce (Kalnajs and Deshler, 2022). The relationship between the maximum scattering amplitude and the optical diameter is referred to as Mie theory (Fig. 3a) and several factors determine the amount of scattered light, including particle size, composition and shape. The index of refraction (n) consists of a real and imaginary part to describe how much the material will scatter and/or absorb light and therefore knowing the predominant particle composition and hence selecting an appropriate n is crucial for accurate determination of optical particle diameters (Sumlin et al., 2018). The primary science objective of the B^2SAP project is to characterize the number size distribution of global stratospheric aerosol. Since the stratosphere is predominantly sulfate aerosols (Bigg et al., 1970; Jäger and Deshler, 2002; Murphy et al., 2021), a bulk index of refraction for pure sulfuric acid ($n = 1.45 + 0.00i$) is used. Mie-derived optical diameters assume that the aerosol is spherical, which is appropriate for predominantly sulfate aerosol. The Mie scattering relationship (Fig. 3) is monotonic for smaller aerosols (100 – 300nm), however for larger diameters (especially 300 - 600 nm and $>$ 800 nm for $n = 1.45 + 0.00i$) there are non-monotonic regions leading to uncertainties in diameter estimations for larger aerosol. To minimize the uncertainty, amplitudes are binned into diameter bins that encompass the entirety of the non-monotonic region. The diameter bins are evenly log-spaced in amplitude for diameters less than 250 nm in the monotonic region, and diameters greater than 600 nm. For 250 – 600 nm size range bins are manually selected by choosing bin edges that correspond to minima in the Mie curve derivative (dlog(Signal)/d(Dp)), Fig. 3b) in the same manner as in Todt et al. (2023). There are large Mie oscillations for particles $>$1000 nm which lead to large uncertainties in the optical particle diameter estimations. Files processed with this method have 36 bins, the same number as the maximum permitted by telemetry. Caution must be taken when evaluating aerosol diameters in the troposphere since aerosol composition and morphology are more varied.

https://doi.org/10.5194/essd-2026-644
Preprint. Discussion started: 26 August 2026

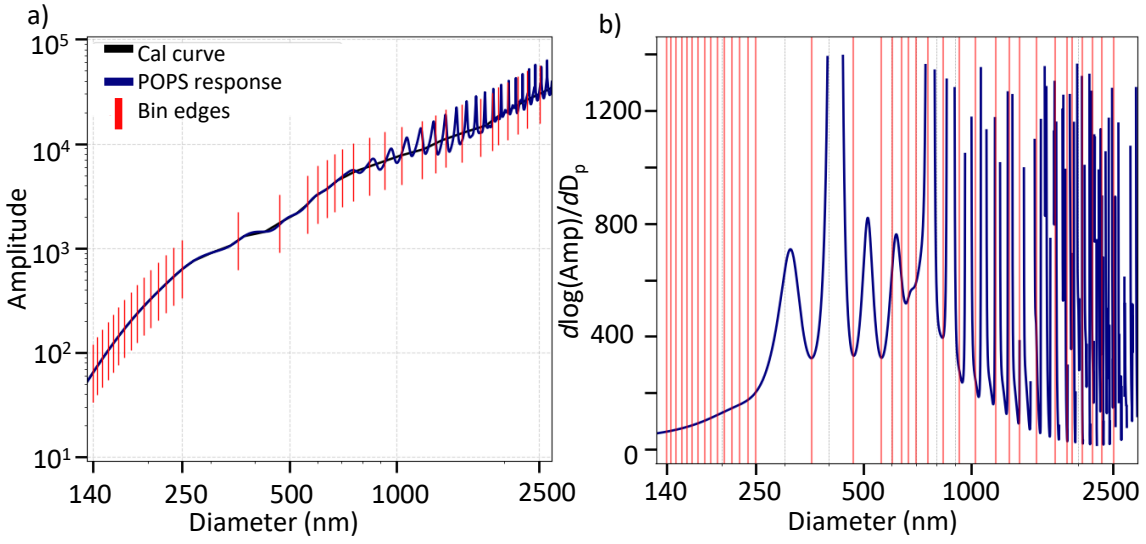

Figure 3. The Mie scattering relationship between maximum scattering amplitude and optical diameter (a) for sulfate aerosols ($n = 1.45 + 0.00i$), used to describe how the amount of light scattered by an individual sulfate particle is related to the diameter of that aerosol. The POPS response for $n = 1.45 + 0.00i$, becomes non-monotonic between 250 - 600 nm and has large Mie oscillations at larger diameters (>1000 nm), so a smoothed calibration function (black) is fit through this response to estimate optical diameter from scattering amplitude. To determine the diameter bin edges (red in both a and b), the derivative of the Mie Curve is used (b), and bin edges are located at minima on this curve to ensure the bins encompass the entirety of non-monotonic regions between 250 – 600 nm.

3.3 POPS Baseline

The POPS baseline is the photomultiplier tube (PMT) signal in the absence of particles, which is primarily the signal generated by stray light and electrical noise. Each second that the POPS is running a baseline is calculated by averaging 16 short segments with no detected particles of the signal. A typical POPS baseline lies between 1950 - 2300 (unitless), with the majority of POPS displaying a baseline of approximately 2100 when pulling laboratory air through the inlet. The baseline standard deviation (BSD) typically ranges between 6 - 10 (unitless), meaning that a peak must have a height of at least 30 to meet the 3σ threshold to be detected as a particle. The maximum baseline standard deviation recorded during the last second (typical value range 7 - 15) is used in combination with the baseline standard deviation as a measure of the POPS noise. The frequency of the noise in the POPS baseline is much higher relative to the width of a particle producing a signal of 50, leading to high confidence in 3σ peak identification. A high baseline might be due to misalignment of the laser leading to increased stray light or potentially due to a large amount of electrical noise which is predominantly from current being converted to a voltage by the A-D converter. Since the noise is a key part of POPS peak detection, POPS instruments that display too high noise (either BSD > 10, or maximum BSD over 1 sec > 13) whilst running in the laboratory are not used in B^2SAP launches as this indicates there is an issue with the optics or electronics and there is a greater uncertainty associated with the detection efficiency of peaks.

https://doi.org/10.5194/essd-2026-644
Preprint. Discussion started: 26 August 2026

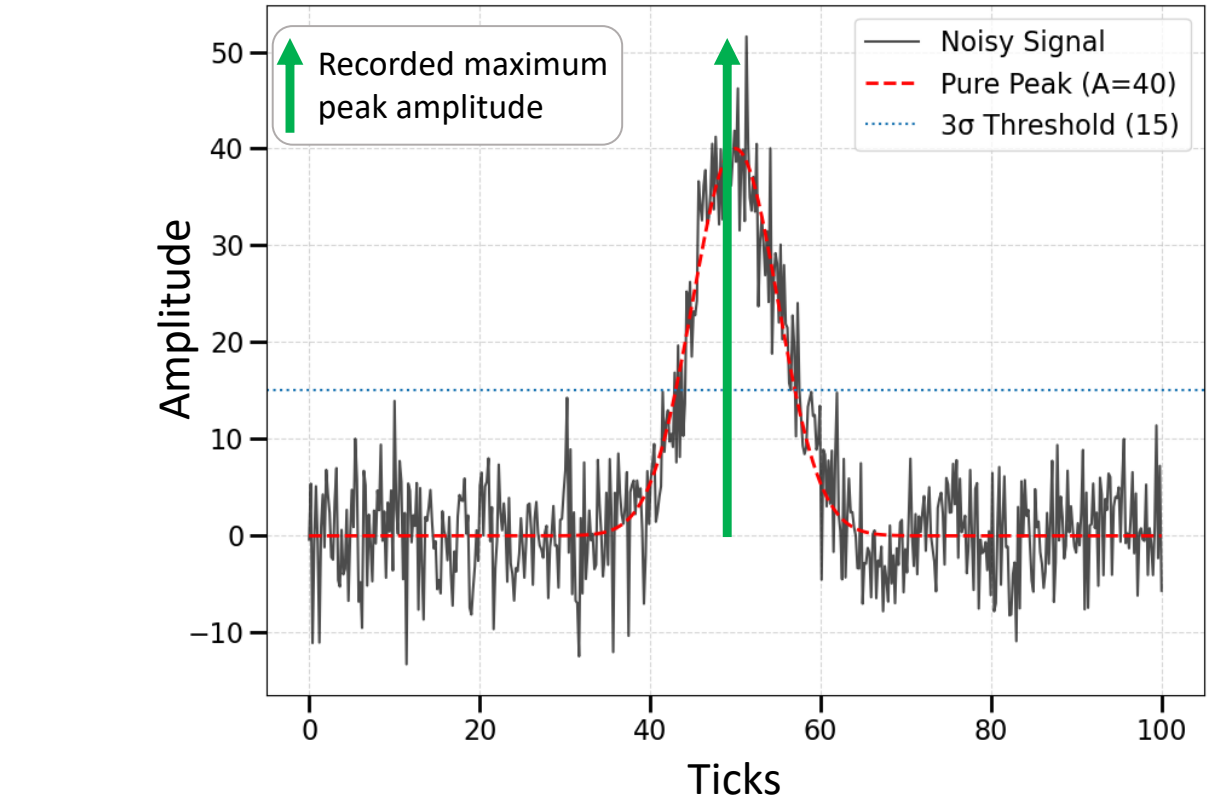

Figure 4. An example of a peak with an amplitude of 40 (red dashed). The baseline has a standard deviation of 5, so to be identified as a peak the particle must scatter light and produce a scattering amplitude of greater than 15 (3σ threshold dotted blue line). The maximum scattering amplitude is the highest point of the peak, so would be identified as the green arrow, and would be recorded as 47 in this example.

It is crucial to correctly determine the POPS baseline as a detected particles peak amplitude is defined as the distance between the average baseline and the tallest part of the scattering peak (the maximum scattering amplitude). As seen in Fig. 4, this means that the maximum scattering amplitude is the result of the peak height plus the POPS noise. This increase is significant for smaller particles with a maximum amplitude that is only just larger than 3σ of the baseline. Due to slight manufacturing and component differences, each POPS instrument is slightly different and there can be variability in POPS-to-POPS performance, with some POPS producing higher baseline standard deviation (BSD). To account for noisier POPS and ensure the optical particle diameter is not overestimated due to this additive BSD effect, the relationship between scattering amplitude and particle diameter is adapted for POPS instruments that display noisier signals (Fig. 5).

The sizing of larger particles ($>$ 200 nm) is not significantly impacted by increasing levels of noise, since the signal-to-noise ratio is already large enough to distinguish between a signal and the background noise, and the addition of BSD on top of the maximum scattering amplitude is a smaller fraction of the actual peak height. During a balloon flight, the BSD typically decreases with increasing altitude due to decreasing atmospheric density contributing less background Rayleigh scattering.

https://doi.org/10.5194/essd-2026-644
Preprint. Discussion started: 26 August 2026

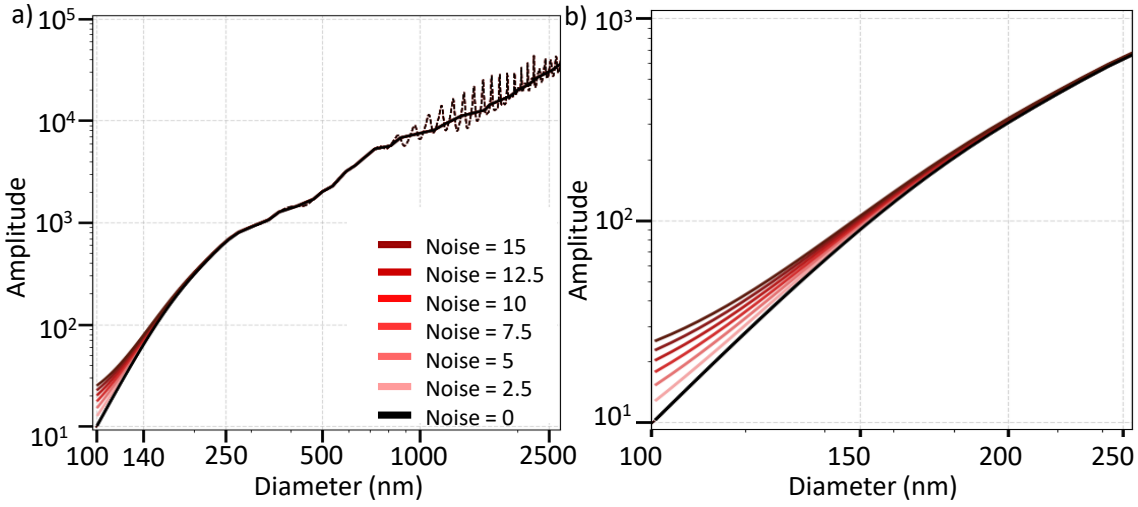

Figure 5. Larger particles are less impacted by increasing levels of noise (a) but there are differences in the Mie Curve for particles with optical diameters of 200 nm or smaller (b), the size range for most stratospheric aerosols. The performance of each POPS instrument is variable and they exhibit differing amounts of noise, which can impact the relationship between scattering amplitude and particle optical diameter (a), especially for the smaller diameter size range (b). The average BSD for a POPS above 200 hPa during a launch is calculated, and the noise level from 0, 2.5, 5, 7.5, 10, 12.5 and 15 is assigned to that flight. The pure sulfuric acid ($n = 1.45 + 0.00i$) Mie scattering relationship associated with that noise level is applied during the calculation from scattering amplitude to optical particle diameter.

Since the B^{2}SAP network is concerned with stratospheric aerosol, only the BSD at pressures lower than 200 hPa are used to calculate the noise level attributed to the scattering amplitude versus optical particle diameter relationship. For every launch, the average BSD above 200 hPa is calculated and the closest value from noise level = [0, 2.5, 5, 7.5, 10, 12.5, 15] is assigned to that launch (Fig. 5). When computing the optical particle diameter from the scattering amplitude, the Mie curve associated with that noise level is applied, and in this way accounts for the impact of the maximum amplitude being the sum of both the signal from scattered light by the particle and the noise of the POPS instrument.

4 Pre-deployment preparation and calibration

4.1 Hardware

POPS are commercially available from Handix Scientific, and when they arrive at the laboratory they are optimized for stratospheric measurements. The software is updated with the largest change causing the electronics to bin particles into 36, rather than 15, diameter bins for the telemetered data. Fürgut (https://www.fuergut.com/en/) pumps are used as these have improved performance at the lower pressure levels, and a switch is mounted on the main PCB to allow the POPS to be switched on whilst it is inside the foam launch box. A thermistor is included and copper-taped to the LFE for temperature corrected flow

https://doi.org/10.5194/essd-2026-644
Preprint. Discussion started: 26 August 2026

calculations. The POPS is securely mounted in a protective foam box, to protect the electronics from the harsh stratospheric conditions and to limit damage upon landing.

4.2 POPS performance

Every POPS is checked in the laboratory before being used as part of a B^{2}SAP payload. These checks are also performed after a launch to identify which POPS can be reused. The instrument is turned on and ran to ensure it meets the baseline is steady, and the BSD is < 10 on the bench. A HEPA filter is placed over the POPS inlet to ensure the aerosol count drops to zero, and there are no leaks. A full flow calibration and gain check are also completed, see Section 4.3.

4.3 Flow calibration and gain check

The POPS are calibrated by monodisperse 508 nm polystyrene latex spheres (PSLs) suspended in deionized water. If required, a potentiometer on the PMT is used to adjust the instrument gain so that the POPS response to this nebulized solution is always the same, with the correct POPS size bin being populated. A nebulizer and the 508 nm PSL solution is provided to all B^{2}SAP launch sites so the POPS can be re-checked and the gain re-adjusted a few days before a launch as it can change during shipping.

As part of the POPS preparation in the laboratory a full temperature-corrected flow calibration is performed. A thermistor measures both the LFE and room temperature. The flow as measured by the POPS and by a flow meter (Buck Calibrator) is measured at five different pump voltages. A linear calibration curve is used to set the flow at different pressure levels during a POPS flight to ensure sufficient flow at higher altitudes. The flow is calibrated so at the surface the pump voltages cause 180 $\pm$ 6 mL min^{-1} and 3 ± 0.1 mL s^{-1} as measured by the Buck Calibrator and POPS differential pressure sensor, respectively. At pressures lower than 30 hPa, the POPS pump voltage is set to yield 360 $\pm$ 6 mL min^{-1} and 3 ± 0.1 mL s^{-1} volumetric flow rate. At the external sites, our collaborators will perform the flow spot check, ensuring the surface-level flow thresholds are achieved. If the average flow is outside this limit a full flow calibration, with temperature corrected flow (Eqs. C7, C6) is performed.

5 Data

The procedure for data processing depends upon whether it was possible to retrieve the payload, as the raw data is saved onto an internal μSD card. Where it is not possible to collect the payload only the data transmitted during the balloon flight by the radiosonde is available, and there are limits on the amount of data that can be transmitted.

5.1 Retrieved payloads

Where possible, B^{2}SAP payloads are retrieved after the launch completion. This is advantageous because the equipment can be reused, and the raw binary files on the POPS μSD card can be analyzed, in some cases increasing the resolution of the POPS binning scheme. The binary files are a raw representation of every particle detected by the POPS as every maximum

https://doi.org/10.5194/essd-2026-644
Preprint. Discussion started: 26 August 2026

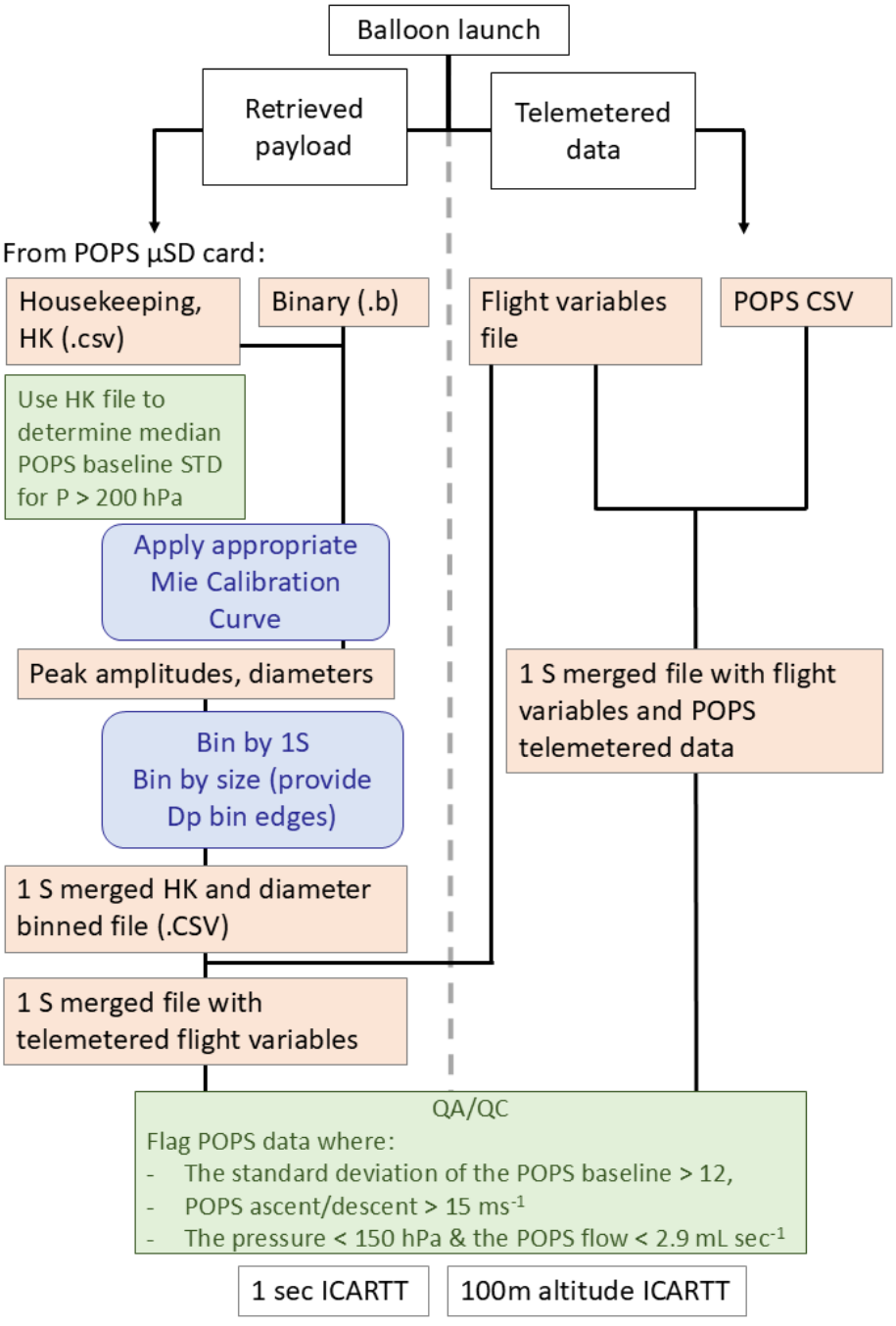

Figure 6. Procedure for generating 1 second and 100m altitude binned ICARTT files for both the retrieved payload, when the raw data on the POPS μSD card is available, and the process when only the telemetered files are saved.

https://doi.org/10.5194/essd-2026-644
Preprint. Discussion started: 26 August 2026

scattering amplitude and the time (in ticks) are recorded, without any assumptions about the particle composition being made, providing more scope for particle analysis. Processing binary files utilises the PyMieScatt Python library (Sumlin et al., 2018), in combination with the atm-py package available on GitHub: https://hagne.github.io/atm-py/. The atm-py code will flag out peaks that fall outside of the calibration range, so amplitudes must be within 53.7 – 31622.8, (equivalent to 53 – 2500 nm, for sulfate particles) during the process of converting the amplitudes to a diameter. The peaks are then averaged into 1 second time bins and the optical diameter is calculated by applying the Mie scattering relationship for sulfate aerosol, $n = 1.45 + 0.00i$, Fig. 3. The diameters are then binned into the diameter bins provided, that were selected to minimize the uncertainty of aerosol sizing by encompassing the non-monotonic regions of the Mie scattering relationship. The time- and diameter-binned peaks are merged with 1S housekeeping files which contain other POPS engineering data.

The Laminar Flow Element (LFE) coupled with the differential pressure sensors provides a pressure - independent measure of volumetric sample flow which is necessary for calculating particle data variables, see Section 5.3. Further information regarding the GPS positional data (altitude, longitude, latitude) and environmental data (RH, temperature, pressure) is provided from the radiosondes attached to the payload and this is also merged to the POPS operational and bins. To ensure accurate time alignment between the radiosonde (GPS time) and POPS datasets (internal clock time), a variable common to both files (POPS flow rate) is used to temporally offset the POPS data relative to the radiosonde. Equations in Appendix C indicate how total aerosol concentration (C1), surface area concentration (C2), volume density (C3), effective radius (C4) and extinction (C5) are calculated from the POPS bins and other variables.

5.2 Telemetered Data

In instances where a retrieval is not possible, the number of bins used to generate scatter-signal distributions is limited by the bandwidth of the data telemetry, Fig. 6. Data is binned by both time (1S) and into pre-configured diameter bins in real-time as part of the POPS software, prior to data telemetry to the receiving station where it is saved. There are constraints regarding the amount of data POPS has allocated for telemetry, so POPS launches that used the iMet-1 or iMet-4 radiosondes could only have 15 diameter bins, plus a few operational variables. For these files, which are from earlier launches or in locations that are hard to access (e.g. South Pole, AQ), 15 bins are reported in the final files. More recent launches use the modernized iMet-54, allowing POPS to have the same selected engineering variables plus 36 diameter bins telemetered to the receiving station. The iMet-54 provides a reliable data link with improved measurement technologies but requires an updated receiving station. The B^2SAP network is in the process of transitioning towards solely using the iMet-54 model but the different launch sites have different transition dates. The data is stored as a .CSV file and merged with the other environmental data from the radiosonde (e.g. GPS co-ordinates, RH, T, P). These CSV files undergo the same QA/QC procedures as the binary files, to produce the archived ICARTT files.

5.3 POPS Data Products in the Archived Files

For every launch, data is archived as both 1 second and 100 m altitude binned formats, regardless of whether it was from the re-processed binary files or the data telemetered during a launch. Where binary files are available the binary file derived ICARTT

https://doi.org/10.5194/essd-2026-644
Preprint. Discussion started: 26 August 2026

files are the preferred choice for archival in the POPS data repository. Archived files include calculated total aerosol concentration (cm^{-3}), surface area concentration (μm^2 cm^{-3}), volume density concentration (μm^3 cm^{-3}), effective radius (μm) and extinction (km^{-1}). Equations C1-C5 show how these data products are derived from the size distribution measurements.

The POPS flow is measured by a differential pressure sensor on the LFE, and this volumetric sample flow is corrected to the ambient temperature (temperature-corrected flow) to get the correct sample volume (Eqs. C6, C7). The count of particles in each bin is divided by the temperature-corrected flow to calculate a number concentration per bin (cm^{-3}). The volumetric sample flow is corrected using the ambient temperature to obtain the correct sample volume (Eq. C7). Total aerosol concentration is determined by summing the number concentration per bin in all size bins that second and indicates how many particles with diameters between 140 – 2500 nm were being detected by the POPS at any given time (Eq. C1). The resulting size distribution provides simultaneous information on both the aerosol number concentration and the aerosol diameter, enabling the characterization of both the aerosol abundance and aerosol optical size within the stratosphere. This information is then used to understand the radiative effects of stratospheric aerosol, and for deriving aerosol micro-physical properties such as surface area concentration (Eq. C2) and volume density (Eq. C3) which governs the availability of surfaces for heterogeneous chemistry (Hazra et al., 2019), with potential implications upon stratospheric ozone layer recovery. Extinction (Eq. C5) is a direct measurement of how quickly radiation is dispersed by absorption and scattering, with an added advantage that this can be compared with results from remote lidar instruments (both satellite and ground-based). The effective radius (Eq. C4) is a measure of the average (mean) diameter of the aerosols, which is crucial for estimating the scattering of incoming solar radiation, since the amount of solar radiation scattered is highly dependent on the size of the particle (Solomon et al., 2011; Murphy et al., 2021).

5.4 ICARTT files

The ICARTT files follow standard ICARTT format. The data are in folders named after launch location and the naming convention for the files is as follows: `NOAA-POPS-B2SAP_GMLBalloon_Location_YYYYMMDD_[datafrequency]_[flightnumber]_R00.ict`. The data frequency is either 100m or 1S, depending on whether the data was binned by 100 m altitude or 1 second time bins. The flight number is a two- or three- letter location designation (see Appendix A Tables A1, A2), followed by the number for that launch. Inside each file is a header explaining details of the file structure, variable descriptions and units (Table C1 and C2).

6 Quality Assurance / Quality Control

Before the files are archived, quality assurance/quality control (QA/QC) is performed to ensure only the highest quality data is archived in the repository. Data where the POPS BSD exceeded 12 is flagged, as well as instances where the ascent/decent rate was greater than 15 ms^{-1}. The POPS relies upon a pump with sufficient flow through the inlet, which is harder to achieve at higher altitudes. As the balloon ascends and pressure decreases the pump efficiency decreases. The flow rate is set to 3 mL s^{-1} at the surface and remains at this flow rate until 200 hPa. As pressure decreases to 200, 150, 100, 75, 50 and 30 hPa the

https://doi.org/10.5194/essd-2026-644
Preprint. Discussion started: 26 August 2026

flow is stepped up to 3.5, 4, 4.5, 5, 5.5 and 6 mL s^{-1}, respectively to ensure the absolute volume of air passing through the POPS is sufficient. Occasionally, the pump cannot maintain the required flow at the highest altitudes and lowest pressures, so the aerosol measurement is more uncertain. At times when the pressure is < 150 hPa and the flow is < 2.9 cc s^{-1} the data is flagged out.

7 Vertical profile

The most frequent launches occur at the Boulder site, and there are over 100 launches where the payload was recovered and the binary files reprocessed to 36 diameter bins. This is sufficient to begin performing statistical analyses to characterize the stratospheric aerosol background for 40 ^{o}N. The vertical profiles in Figure 7, under standard temperature and pressure, depict the aerosol number concentration between 140 - 2500 nm, from 10 km to 29 km altitude, using the 1S ICARTT files. The mean (blue), median (green) and 10^{th} – 90^{th} percentiles (red, dashed) indicate that the most variability in aerosol number concentration that occurs within this size range is observed at or close to the tropopause ($<$ 15 km) which is to be expected since the tropopause height varies and there are more aerosols in the troposphere. Tropospheric intrusions also introduce additional sources of aerosol to the lower stratosphere. The increase in total aerosol concentration at 17.5 km indicates the average altitude of the persistent stratospheric aerosol layer (or Junge Layer (Junge and Manson, 1961; Bigg et al., 1970)) for this latitude. Above 21 km the average aerosol number concentration is uniform with increasing altitude, centered around 50 cm^{-3}. Individual aerosol plumes are observed in a few profiles with elevated number concentrations reaching 600 cm^{-3}, and it is only by truly understanding typical background conditions that we can accurately pinpoint and quantify the increase in aerosols for these plumes.

8 Sensitivity to changing aerosol composition

The optical diameter and radiative impact of SA depends are functions of the aerosol composition, which is represented by the aerosol's refractive index (*n*) and mathematically this is described by Equation 1. The index of refraction is composed of a real (*a*) and imaginary (*b*) part describing the amount the aerosol will scatter versus absorb the incident light (Shin et al., 2024).

$$n = a + bi \tag{1}$$

Altering either component will change the relationship between scattering amplitude and optical diameter and hence the shape of the Mie scattering relationship, although the general principal that larger particles scatter more light remains valid, particularly for the smaller diameter aerosols (Fig. D1 a, c, d). In the archived files, $n = 1.45 + 0.00i$ for pure sulfuric acid was used as stratospheric aerosol is predominantly sulfate. To identify how sensitive the POPS response is to slight changes in aerosol composition which might occur due to the introduction of tropospheric aerosol or stratospheric perturbations the binary files were reprocessed with different *n*-values. Deshler and Kalnajs (2026) showed *n* can vary by 1.5 % throughout the vertical structure of the stratosphere (Deshler and Kalnajs, 2026), and that in the lowermost stratosphere some aerosols contain up to 50% organic material (Martinsson et al., 2019). Examples of events that might perturb the background state of stratospheric aerosol

https://doi.org/10.5194/essd-2026-644
Preprint. Discussion started: 26 August 2026

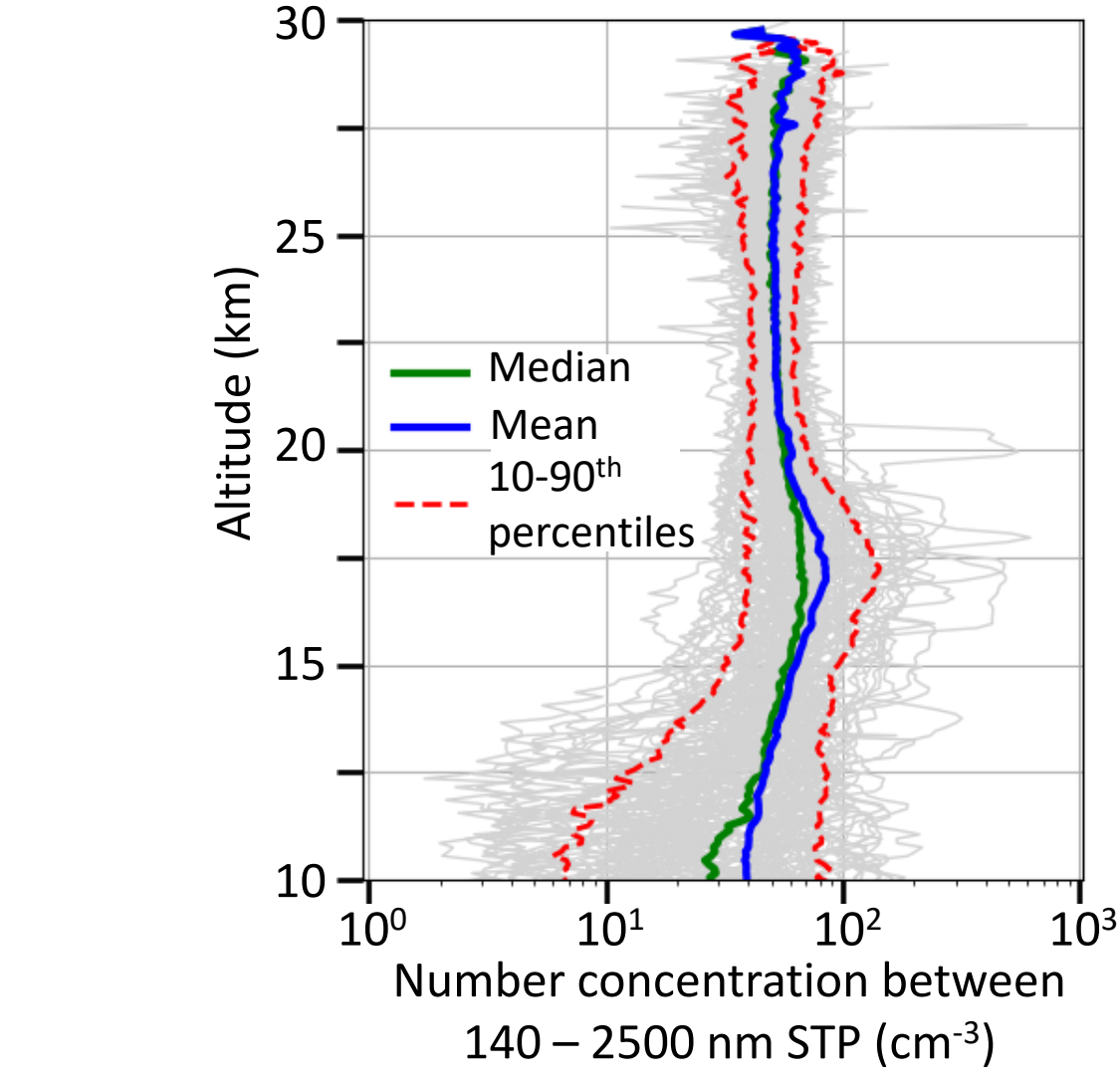

Figure 7. Aerosol number concentration for aerosol with diameters between 140 - 2500 nm under standard temperature and pressure for all Boulder, CO, USA launches (until Feb 2026). Individual aerosol number concentration profiles from the 1S ICARTT files are in grey and the mean (blue), median (green) and 10th – 90th percentiles (red) show the average aerosol concentrations for altitudes between 10 – 30 km.

https://doi.org/10.5194/essd-2026-644
Preprint. Discussion started: 26 August 2026

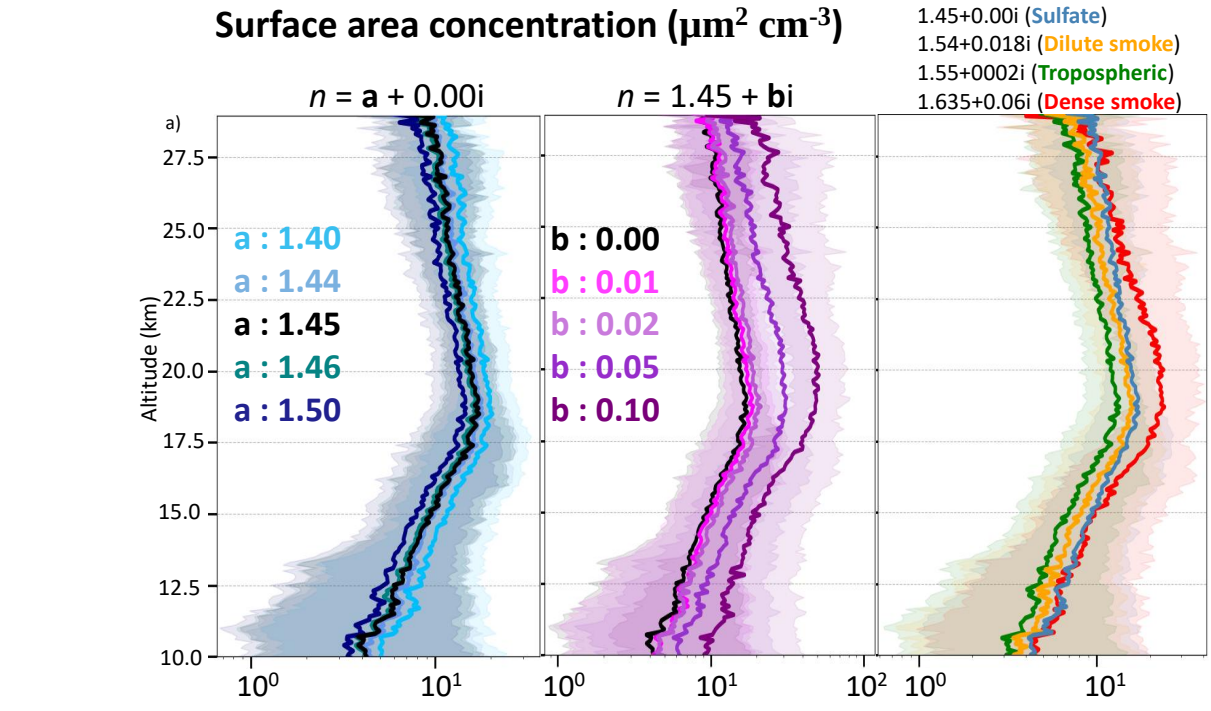

Figure 8. The average (solid line) and 10 - 90^{th} percentiles (shaded area) vertical profile from re-processing 100- binary files with different n-values and associated Mie scattering relationships, to identify how sensitive the POPS data is to changing particle composition. The real portion of n was changed between 1.40 and 1.50 (a), the imaginary portion of n was changed between 0.00 - 0.1 (b) and then n-values for known particle compositions were used in (c). The vertical profiles show how the average surface area concentration for these 100 binary files were computed and a vertical profile.

are; explosive volcanic eruptions injecting material such as gases (SO_2, H_2O, CO_2) and volcanic ash into the atmosphere (Eckhardt et al., 2008; Asher et al., 2023): and large wildfire events have been observed to introduce biomass burning aerosols to the stratosphere (Hooghiem et al., 2020). Therefore, n was changed by incremental amounts to the real and imaginary components (Fig D1a and c) used for pure sulfuric acid, to imitate increasing amounts of different material mixed within the sulfate aerosol. Index of refractions for tropospheric aerosol ($n = 1.55 + 0.002i$, (Aldhaif et al., 2018)), diluted smoke ($n = 1.54 + 0.018i$) and dense smoke ($n = 1.635 + 0.06i$, (Womack et al., 2021)) to emulate concentrated filament of aerosol present in the stratosphere were also evaluated (Fig D1e). For each n investigated, 100 binary files from the Boulder dataset were reprocessed and binned by 36 diameter bins. The median vertical profile (solid line) of the 100 launches, with the 10 - 90th percentiles (shaded region) was used to identify how the alterations in n changed the surface area concentration (Fig. 8) or effective radius (Fig. 9) vertical profile. The same 100 binary files were reprocessed with different n, to identify the sensitivity of POPS data products such as surface area (Fig 8) and effective radius (Fig 9) to the aerosol composition. When the real component of n was changed between 1.40 - 1.50, but the imaginary component was fixed at 0.00i, there were changes to the Mie scattering relationship

https://doi.org/10.5194/essd-2026-644
Preprint. Discussion started: 26 August 2026

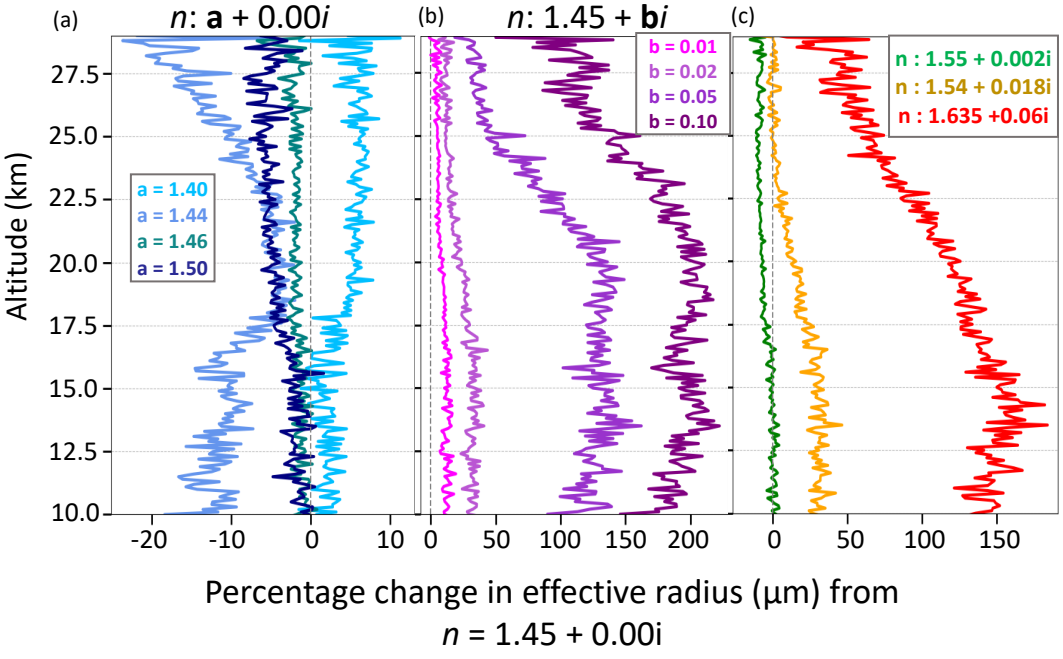

Figure 9. The percentage change in effective radius from using an index of refraction reflective of pure sulfuric acid ($n = 1.45 + 0.00i$) between 10 - 29 km, when the index of refraction was changed by the real component (a), imaginary component (b) and to reflect different aerosol compositions (c).

(D1a) which impacted the the smaller optical diameters (140 - 500 nm) more than the larger diameters. The Mie scattering relationships are shown as amplitude on y-axis and optical diameter on the x-axis, and as *a* increased from 1.4 to 1.5, each incremental Mie curve sat higher, leading to smaller diameters calculated for the same amplitude (Fig. D1b). Subsequently, the surface area concentration vertical profile (Fig. 8) looked similar for all scenarios, with small decreases in the surface area concentration over all altitudes investigated, as *a* increased. The effective radius was within 10% of the value calculated for pure sulfuric acid (Fig. 9a) . The Mie scattering relationships vary much more when the imaginary part of *n* is increased (Fig. D1c), particularly for the larger diameter particles (>300nm). As *b* increased, the Mie curve in Fig. D1d sits lower, so that for a fixed amplitude, the calculated optical diameter would be larger for higher *b*-values. Increasing the imaginary portion of *n*, had a more significant impact upon the median surface area concentration profile when the 100 binary files were reprocessed with the different Mie curves relating to the indices of refraction investigated. Using *n*-values with an imaginary component greater than 0.02, caused large increases in the surface area concentration (Fig 8b) relative to the pure sulfate scenario. This was also translated into elevated effective radii by 200% at altitudes between 10 - 20 km (Fig 9b). Note that this *b* value would indicate a large proportion of the aerosol is strongly absorbing, and would only be used for dense smoke plumes. The imaginary component has greater impact on optically sizing aerosol.

https://doi.org/10.5194/essd-2026-644
Preprint. Discussion started: 26 August 2026

Changing the index of refraction to simulate different aerosol types, is representative of when the B^{2}SAP payload intercepts a dense plume of material where both the real and imaginary components change simultaneously. The same process was used, where the median and 10 - 90th percentiles were generated from the same 100 binary files using different indexes of refraction to represent tropospheric, dilute smoke and dense smoke throughout the vertical profile. When *n* reflects tropospheric aerosol, the median surface area concentration and effective radius vertical profiles were very similar to the sulfate aerosol scenario. The *n*-values for dilute and dense smoke both have an imaginary part, and hence there a significant diversions from the median sulfate vertical profile. The Dense Smoke scenario, where $n = 1.635 + 0.06i$, has the largest imaginary component, which led to the greatest increase in surface area concentration. This elevated surface area concentration was accentuated between 16 - 25 km, where the Junge Layer is expected to be located for 40^{o}N and an effective radius that was elevated by 100 - 150 % at altitudes below 22.5km (Fig.9c). For instances where a concentrated plume of known aerosol material is being transported throughout the stratosphere, changing the index of refraction to reflect the aerosol composition would better account for the radiative impact that the aerosol perturbation would have on the surface.

8.1 Sensitivity to different number of diameter bins

To investigate the POPS sensitivity to the bin edge locations and number, different binning schemes were applied to reprocess 113 binary files, for a sulfate index of refraction. Similarly to the index of refraction sensitivity analysis (Section 8), the median size distribution for each binning scheme was computed over all files in this analyses. Figure 10 compares the $dS/dlogDp$ over 140 - 2500 nm diameter for the 19 - 21 km altitude range. Where only the telemetered data is available, the POPS relies on the preset diameter size bins, set in the configuration file. Historically, 15 bins were used for telemetered data, with 36 bins becoming the norm with the use of the iMet-54, which allows a larger amount of data to be sent. For one intensive balloon launch deployment the POPS had 20 aerosol size bins telemetered back to the receiving station. In the 'Evenly log spaced' scenario the bins were also evenly log spaced by amplitude for 15, 36 and 50 bins. Additionally, there were 15 and 36 binning schemes where the minima of the derivative of the Mie scattering relationship were manually selected between 250 - 600 nm, to encompass the non-monotonic regions of the Mie curve (labeled 'Derivative minima'), as for Todt et al. (2023). All the binning schemes look similar for the smaller diameter aerosols (140 - 250 nm), where the Mie scattering relationship is monotonic and steep. One of the strengths of the POPS instrument is the ability to detect particles as small as 140 nm diameter, one of the lowest detection limits for low cost aerosol instrumentation, and allowing the instrument to capture the more abundant stratospheric aerosol mode. The POPS is insensitive towards changing bin placement for this size range. There is much more variability in the $dS/dlog(d_P)$ signal for each binning scheme for aerosols with a diameter greater than 250 nm. The 50 and 100 binning schemes (Fig. 10 pink and purple) over sample the aerosol for at least two bins between 300 - 400 nm and 450 - 500 nm. This is the region whee the Mie curve shows non-monotonicity so the amplitudes which correspond to multiple diameters are being counted in the smaller of the bins, leading to the elevated surface area followed by a depleted consecutive size bin. Providing the band width is available it could be advantageous to have a larger number of bins as this could allow oversampling and then the application of different *n*-values, even for telemetered data. This sensitivity analysis indicates that greater than 100 bins would be required to do this. The 15 bin telemetered and evenly log spaced binning schemes are more

https://doi.org/10.5194/essd-2026-644
Preprint. Discussion started: 26 August 2026

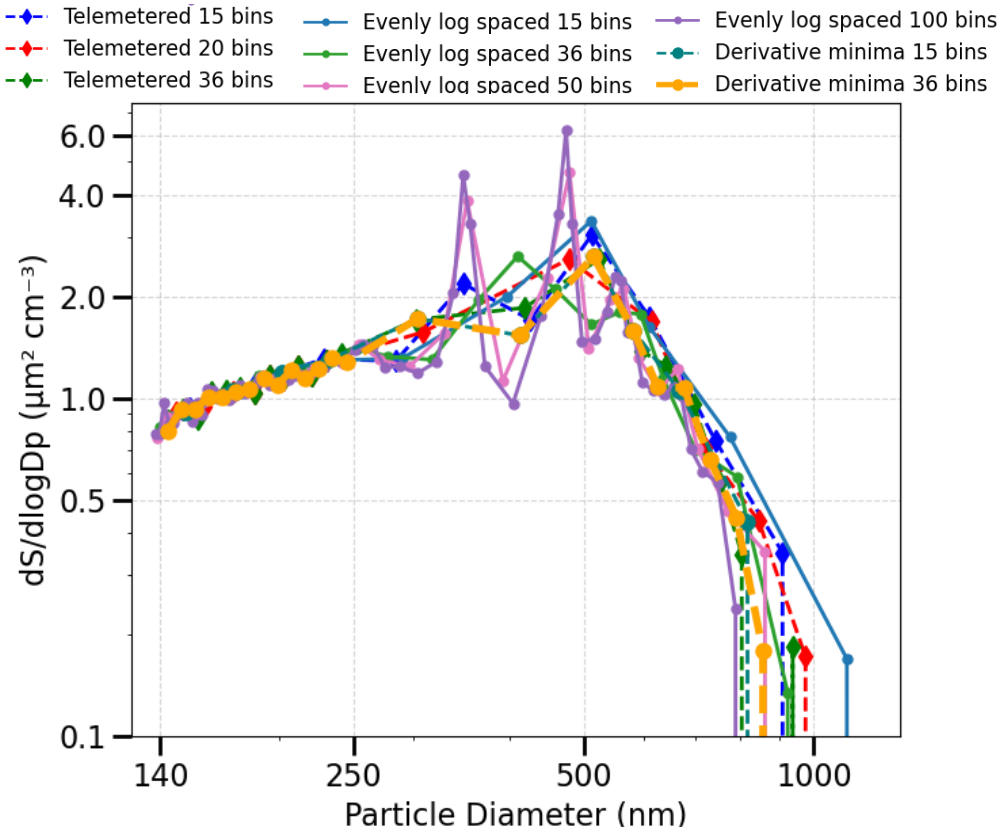

Figure 10. The surface area concentration size distribution for between 19 - 21 km altitude was computed for the reprocessed binary files when different diameter bin edges were used to bin the optical particle diameters.

variable, suggesting that more bins are required, or strategically selected to fully capture the aerosol size distribution. The 15 bin evenly log spaced scheme indicates the presence of larger particles $> 1000nm$ where no other scheme did, so this bin edge must encompass a Mie oscillation that artificially pulls the median diameter size up. The 20- and 36- bin telemetered schemes are able to represent the aerosol size distribution well across the full size distribution. Where diameter bin edges were selected to entirely cover the full size range of the non-monotonic regions of the Mie Curve (Fig 10 teal and gold) exhibits a relatively smooth curve in the size distributions and sit sin the middle of these different binning schemes, providing high confidence that this is close to the true value and does not over or under sample aerosol in any one size bin, especially within the non-monotonic region.

https://doi.org/10.5194/essd-2026-644
Preprint. Discussion started: 26 August 2026

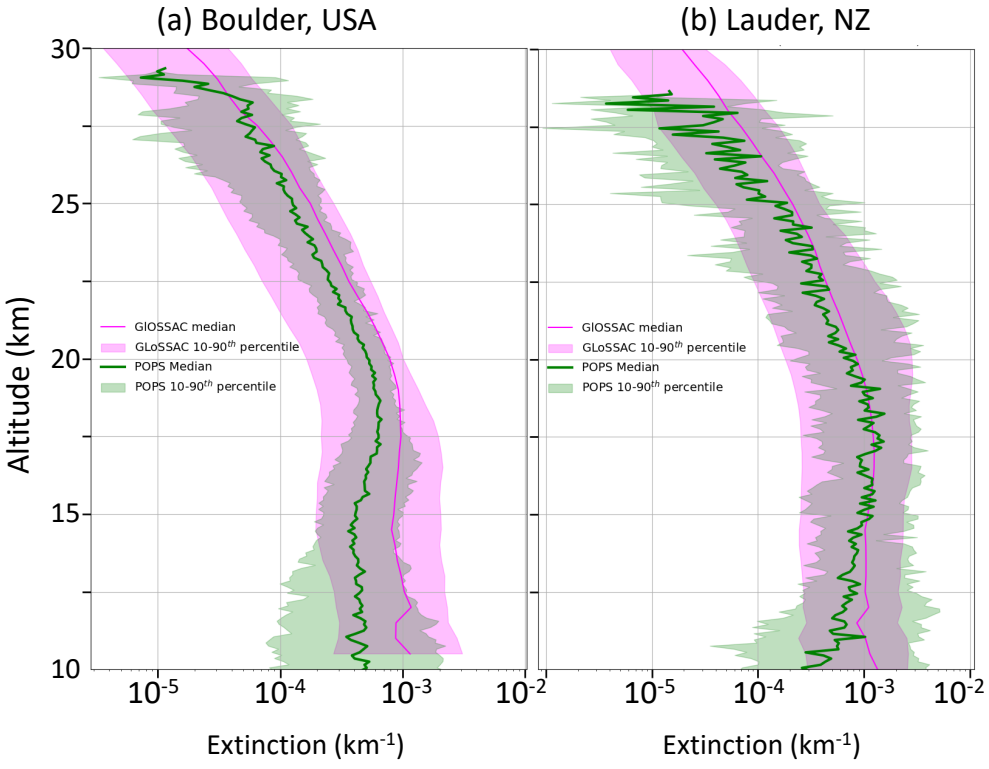

Figure 11. Median GloSSAC v2.23 aerosol extinction at 525 nm for a) 38.5 - 42.5 ^{o}N (Boulder) and b) 42.5 – 47.5 ^{o}S (Lauder, NZ), between 2019 - 2024 (solid pink line), overlaid with median POPS aerosol extinction at 532 nm from Boulder, CO (40 ^{o}N) launches that occurred between 2019 – 2024 (solid green line). The 10 - 90th percentiles for both GloSSAC and POPS extinction are shown as pink and green shaded areas, respectively.

9 Comparison with GloSSAC

The Global Spaced Based Stratospheric Aerosol Climatology (GloSSAC, https://www.earthdata.nasa.gov/data/projects/glossac) product is a NASA assimilation of direct stratospheric aerosol observations from a variety of satellites and models e.g. Stratospheric Aerosol and Gas Experiment III (SAGE-III) to produce a timeline of stratospheric aerosol extinction coefficients from 1970 – December 2024 (version 2.23) for four different wavelengths, 386, 452, 525 and 1020 nm. The GloSSAC extinction (Fig. 11, purple) at 525 nm, from 01-01-2019 was used to compare with the POPS extinction calculated with a wavelength of 532 nm. The GloSSAC record is a monthly measurement which assumes longitudinal homogeneity. For this comparison the latitudes ±2.5 degrees of Boulder (40 ^{o}N) and Lauder, NZ (45^{o}S) were selected, between 10 – 28 km altitude. The POPS-derived extinction (green) is the median of all the POPS vertical profiles, with the 10-90th percentiles also shown in Fig. 11. The shape and variability of the POPS extinction profiles closely match the GloSSAC observations, especially for altitudes above 17.5 km. GloSSAC observations will have increased uncertainty for lower altitudes due to changing tropopause

https://doi.org/10.5194/essd-2026-644
Preprint. Discussion started: 26 August 2026

heights. However, there is still very good agreement between the Boulder and Lauder vertical profiles at these altitudes which is especially promising for the southern hemisphere during a hugely perturbed southern hemisphere stratosphere. The POPS also has higher vertical resolution for any given launch, which adds to the variability in the Boulder measurements, and the smoother appearance of the GloSSAC record. The median Lauder (Fig. 11b) POPS extinction was derived from 20 profiles, rather than the 99 profiles used to calculate the Boulder extinction median, hence the increased variability. The Hunga-Tonga eruption occurred during this time period (2021) and this perturbed the Southern Hemisphere stratosphere more, and for longer than the Northern Hemisphere stratosphere. Both the POPS extinction and GloSSAC extinction measured this elevated aerosol extinction coefficient.

10 Conclusions

This study establishes the B^2SAP network as a unique set of stratospheric aerosol observations that are critical for understanding both the typical background abundances and variability of the stratospheric aerosol layer. Through a comprehensive evaluation of the POPS, including its detection theory, instrument baseline and noise characteristics and calibration procedures, it was demonstrated that this instrument is optimal for the optical detection of stratospheric aerosols and hence the B^2SAP network. The strength of using the POPS instrument to calculate aerosol number concentrations and size distributions is that very few balloon-borne aerosol instruments are able to accurately detect particles as small as 140 nm diameter, capturing more of the dominant stratospheric aerosol size range and resulting in a more complete picture of aerosol in the stratosphere. The strategically located launch sites are essential for the assessment of global stratospheric aerosol, with the deep tropical sites being especially important as there is a historic lack of observations in this region. Since two sites, one in the Northern and one in the Southern mid-latitudes have had on-going launches since 2019, analysis of the B^2SAP network allows both the spatial and temporal (multi-year and short term) variability in stratospheric aerosol to be quantified. B^2SAP observations complement and expand upon existing aerosol measurements made by long term ballooning efforts and aircraft by providing regular, vertically resolved aerosol size distributions that bridge the gap between intensive field campaigns and reaching higher into the stratosphere. These observations are a benchmark for constraining aerosol models, improving global radiation estimates, and validating lidar and satellite-based retrievals. By establishing the natural variability of the background stratospheric aerosol layer, the B^2SAP dataset improves our ability to detect and quantify natural and anthropogenic perturbations, including volcanic eruptions, wildfire smoke injections, and future climate intervention scenarios such as stratospheric aerosol injection. Together with the portability of the POPS instrument and the expanding global observing network, B^2SAP provides a foundation for both long-term monitoring and rapid-response measurements of future stratospheric aerosol events.

11 Data availability

This aerosol data is publicly available from the B^2SAP website at https://csl.noaa.gov/projects/b2sap/data.html. The B^2SAP dataset also has an NCEI DOI of : 10.25921/mchy-y552, (Smith et al., 2026)

https://doi.org/10.5194/essd-2026-644
Preprint. Discussion started: 26 August 2026

Open Access Earth System Science Data Discussions

Appendix A: Geographic Information

The B^2SAP/GlO_3W payloads are launched from a variety of sites across the globe. Collaborators receive calibrated and prepared instruments to perform some last-minute checks and then launch on our behalf. Sites designated as having frequent launches aim to have a payload launched every 2 – 3 months (Table S1), other sites are more opportunistic (Table S2).

Table A1. Regular B^2SAP launch sites and the number of launches completed as of June 2026.

Code	Launch site	Latitude (°N)	Longitude (°)	Launches
bu	Boulder, CO, USA	39.9	-105.2	136
bw	Utqiagvik, AK, USA	71.3	-156.6	11
hh	Hilo, HI, USA	19.5	-155.6	20
la	Lauder, New Zealand	-45.0	169.7	34
par	Paramaribo, Suriname	5.9	-55.2	4
po	Koror, Palau	7.3	134.5	2
rn	La Réunion Island, France	-21.1	55.4	19
sp	Amundsen–Scott South Pole, Antarctica	-85.0	0.0	6

Table A2. Opportunistic based B^2SAP launch sites and the number of launches completed as of June 2026.

Code	Launch site	Latitude (°N)	Longitude (°)	Launches
ri	Amundsen Scott Base, Antarctica	-77.8	166.8	4
sj	San Jose, Costa Rica	9.9	-84.0	1

Appendix B: Portable Optical Particle Spectrometer (POPS)

The main physical components of the POPS instrument are: a brass inlet to sample the air, a laminar flow element (LFE) to accurately measure the volume of air sampled, an optical chamber containing the laser, a photomultiplier to detect scattered light, and a pump to pull air through the optical chamber. The POPS is constructed to ensure the sampled air flow moves in a straight line through the inlet, LFE and optical chamber. The sampled air flow passes through the inlet and nozzle which transforms the flow of air to a 1 mm diameter jet flow that enters the optical chamber where it is intersected by laser light at a perpendicular angle to the jet flow direction. This light is generated from a laser diode (405 nm), and has been collimated and focused by a series of lenses, with apertures used to select the most intense part of the beam and reduce stray light (Fig. B1). The resulting laser beam has a height of 1.3 mm, fully encompassing the jet flow (1 mm diameter) which contains the particles.

https://doi.org/10.5194/essd-2026-644
Preprint. Discussion started: 26 August 2026

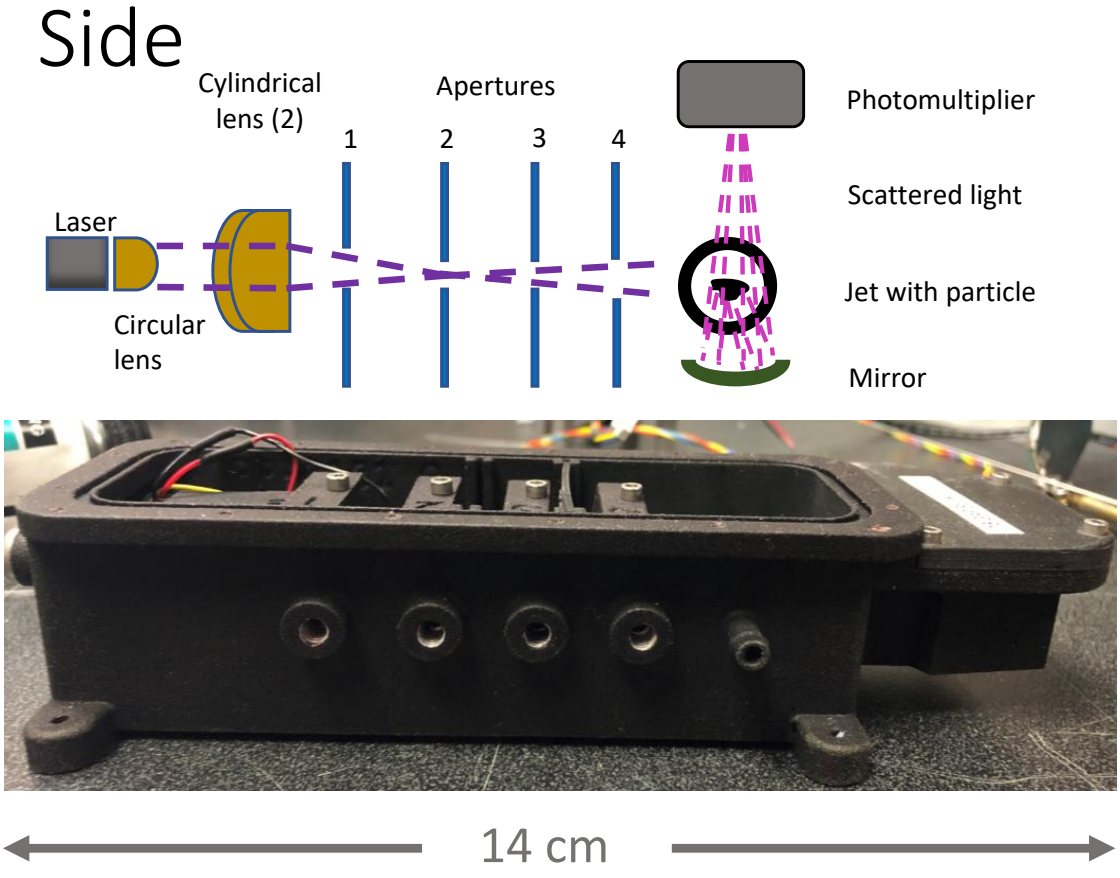

Figure B1. The POPS optical chamber contains a 405 nm laser diode, and a series of lenses and apertures to focus the light to a 1.3 nm high region that intersects the sampled air flow containing the particles to be detected. The sampled air flow travels through the optical chamber and exits from the exit that protrudes on the right hand side. This is connected to a pump that pulls air through the optical chamber.

Individual particles in the jet flow scatter the laser light, and the sideways scattering fraction is reflected by the spherical mirror towards the photomultiplier tube (PMT) producing an electrical current proportional to the light received. This current is converted to a digital voltage and the POPS software identifies these changes in voltage as a pulse signal with associated arrival time, peak height, and peak width.

Appendix C: POPS variables and data products in ICARTT

C1 Equations

The POPS data products of aerosol number concentrations, surface area concentration, volume density, effective radius and extinction are derived from the following calculations.

https://doi.org/10.5194/essd-2026-644
Preprint. Discussion started: 26 August 2026

Open Access Earth System Science Data Discussions

i) total aerosol number concentration between 140 - 2500 nm (TAC, cm^{-3}, C1).

$$TAC = \sum_{i=1}^{N} \frac{n_i}{Q} \tag{C1}$$

where *N* is the number of bins, *n* is the count of aerosol within that bin and *Q* is the volumetric temperature corrected sample flow rate (cm^{-3}).

ii) surface area concentration (SAC, $\mu m^2 cm^{-3}$), C2

$$SAC = \sum_{i=1}^{N} \frac{n_i}{Q} \pi r^2 \tag{C2}$$

Where *r* is the aerosol radius in nm, and for this and the following equations that use *r*, it is the median radius for each diameter bin.

iii) volume density (VD, $\mu m^3 cm^{-3}$), C3)

$$VD = \sum_{i=1}^{N} \frac{n_i}{Q} \frac{4}{3} \pi r^3 \tag{C3}$$

iv) effective radius (ER, μm, C4)

$$ER = 3 \frac{VD}{SAC} \tag{C4}$$

and v) aerosol extinction coefficient (EXT, km^{-1}, C5) at 532 nm wavelength. The aerosol extinction coefficient is determined by integrating Mie theory over the particle size distribution and the equation below is applied using the PyMieScatt python package.

$$\beta_{\text{ext}}(\lambda) = \sum_{i=1}^{N} N_i \, \sigma_{\text{ext}}(D_i, \lambda, m), \tag{C5}$$

where β_{ext} is the extinction coefficient (km^{-1}), N is the number concentration in bin *i*, D_i is the bin midpoint diameter, *m* is the complex refractive index and σ_{ext} is the Mie extinction cross-section.

The POPS temperature (T_{POPS}) is corrected using ambient temperature from the radiosonde (T_{Rad}), Equation C6.

$$T_{POPS} = \frac{T_{Rad} + 273.15}{T_{POPS} + 273.15} \tag{C6}$$

The POPS temperature (T_{POPS}) is applied to the POPS sample flow (q) then used to temperature correct the volumetric sample flow (Q).

$$Q = q.T_{POPS} \tag{C7}$$

https://doi.org/10.5194/essd-2026-644
Preprint. Discussion started: 26 August 2026

C2 ICARTT data

Variables included in the ICARTT files, with their units and the descriptions. ICARTTs with 15, 20 or 36 POPS bins will only contain the relevant number of bins. The bins size range is subject to the configuration file used in telemetry or the selected bin edges used in data that has been re-binned, so it is crucial to read each file's header information to obtain the most accurate conclusions regarding optical particle size. The table below provides information on the variables and their descriptions found in the ICARTT files, however, please note that the values for bin edges change depending on the bin edges used for that specific file.

Table C1. Variables and descriptions for ICARTT files used in the B^2SAP dataset.

Variable	Unit	Description
TIME_START	s	Start time of 100 m altitude bin in seconds since midnight UTC on day of flight
TIME_STOP	s	End time of 100 m altitude bin in seconds since midnight UTC on day of flight
TIME_MID	s	Mid time of 100 m altitude bin in seconds since midnight UTC on day of flight
Alt_km	km	GPS-reported altitude above sea level
Lon	deg	GPS-reported longitude
Lat	deg	GPS-reported latitude
Press_mb	mb	Ambient atmospheric pressure measured at payload altitude
Temp_C	°C	Ambient atmospheric temperature measured at payload altitude
Theta_K	K	Potential temperature of ambient air
Aerosol_concentration	cm^{-3}	Aerosol number concentration between 140 - 2500 nm
Surface_Area_Conc	$\mu m^2\ cm^{-3}$	Surface area concentration between 140 - 2500 nm
Volume_density	$\mu m^3\ cm^{-3}$	Volume density between 140 - 2500 nm
Effective_radius	μm	Effective radius
Extinction	km^{-1}	Aerosol extinction coefficient
15, 20, 36 bin columns	cm^{-3}	Particle number concentration in size bins
POPS LFE temp ^oC	^oC	Laminar flow element (LFE) temperature

Appendix D: Sensitivity Analysis

A scattering amplitude of 1000 was used in all scenarios to estimate the optical particle diameter (S1 b, d, f) to emphasize the impact of changing the assumption of the particle composition (*n*-value). The largest deviation to the relationship between scattering amplitude and optical particle diameter occurred when the imaginary part of *n* was changed to 0.1 (S1c). The sensitivity of the POPS to different refractive indices, or aerosol composition was investigated by systematically changing the (a) real, (b) imaginary, or (c) both using *n* from literature and applying these when 100 binary files were reprocessed. An index

https://doi.org/10.5194/essd-2026-644
Preprint. Discussion started: 26 August 2026

Table C2. The bin information changes depending on the binning scheme used to archive the data. This is an example of a file that had was archived under the telemetered 36 bins. These columns would all be inserted into the file in the location of the 'Bins' column in Table C1.

Bin name	Unit	Size range for number concentration
Bin01	cm^{-3}	140–146.14 nm
Bin02	cm^{-3}	146.14–152.56 nm
Bin03	cm^{-3}	152.56–159.25 nm
Bin04	cm^{-3}	159.25–166.24 nm
Bin05	cm^{-3}	166.24–173.54 nm
Bin06	cm^{-3}	173.54–181.16 nm
Bin07	cm^{-3}	181.16–189.11 nm
Bin08	cm^{-3}	189.11–197.41 nm
Bin09	cm^{-3}	197.41–206.07 nm
Bin10	cm^{-3}	206.07–215.12 nm
Bin11	cm^{-3}	215.12–224.56 nm
Bin12	cm^{-3}	224.56–234.41 nm
Bin13	cm^{-3}	234.41–244.70 nm
Bin14	cm^{-3}	244.70–361.30 nm
Bin15	cm^{-3}	361.30–472.80 nm
Bin16	cm^{-3}	472.80–567.00 nm
Bin17	cm^{-3}	567.00–610.66 nm
Bin18	cm^{-3}	610.66–657.69 nm
Bin19	cm^{-3}	657.69–708.33 nm
Bin20	cm^{-3}	708.33–762.88 nm
Bin21	cm^{-3}	762.88–821.62 nm
Bin22	cm^{-3}	821.62–884.89 nm
Bin23	cm^{-3}	884.89–953.03 nm
Bin24	cm^{-3}	953.03–1026.42 nm
Bin25	cm^{-3}	1026.42–1105.46 nm
Bin26	cm^{-3}	1105.46–1190.59 nm
Bin27	cm^{-3}	1190.59–1282.27 nm
Bin28	cm^{-3}	1282.27–1381.01 nm
Bin29	cm^{-3}	1381.01–1487.36 nm
Bin30	cm^{-3}	1487.36–1601.89 nm
Bin31	cm^{-3}	1601.89–1725.25 nm
Bin32	cm^{-3}	1725.25–1858.10 nm
Bin33	cm^{-3}	1858.10–2001.18 nm
Bin34	cm^{-3}	2001.18–2155.28 nm
Bin35	cm^{-3}	2155.28–2321.25 nm
Bin36	cm^{-3}	2321.25–2500 nm

https://doi.org/10.5194/essd-2026-644
Preprint. Discussion started: 26 August 2026

of refraction of $1.45 + 0.00i$ for pure sulfuric acid is used for the archived files, and the real component of this was altered to 1.40 - 1.50 (SD1 a) to investigate the impacts of changing particle composition. Subsequently, the imaginary component was changed from 0.00 to 0.1 (SD1 c) to investigate the impact of changing this part of the *n*-value. Finally, *n*-values that are representative of different aerosol types, sulfate, generic tropospheric aerosol, diluted smoke and dense smoke (SD1e) were applied to the binary files to see how the POPS data products are impacted if there were a large plume of aerosol traveling through the stratosphere.

Author contributions. KS, AB, TT, and JS are responsible for the B2SAP project operationally, and preparing POPS instrumentation. EA, EH, PC, and AF are responsible for balloon launches, the GlO3W instrumentation, and telemetry. HT developed the atm-py code used to process the POPS binary files. All remaining authors are external collaborators who launched B2SAP/GlO3W payloads from locations outside Boulder.

Competing interests. No competing interests are present.

Acknowledgements. This research was supported by the NOAA Earth's Radiation Budget (ERB) Program, Award 140301010001. Kate Smith and Alex Baron would like to acknowledge Reflective for supporting this research through their Fellowship program.

https://doi.org/10.5194/essd-2026-644
Preprint. Discussion started: 26 August 2026

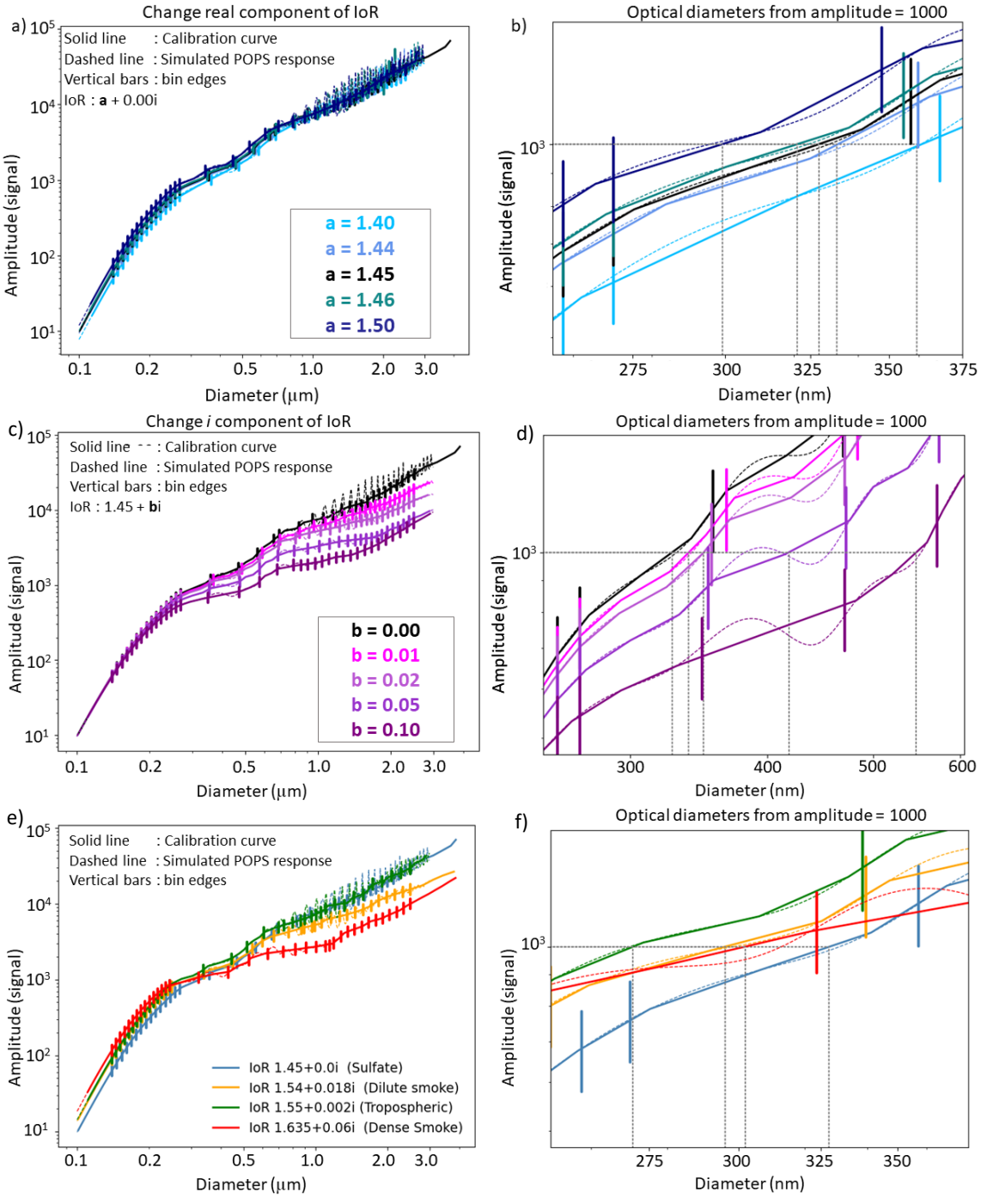

Figure D1. The relationship between the scattering amplitude and the optical particle diameter changes (Mie Curve or Mie scattering relationship) as the real (a) and imaginary (c) components of the index of refraction are varied. The Mie curves have a different shape when the relationship was evaluated for *n*-values associated with different aerosol compositions (e). The different Mie Curves lead to different optical diameter estimations for a fixed amplitude (e.g. of 1000) across all the *n* investigated in this study (b,d,f).

https://doi.org/10.5194/essd-2026-644
Preprint. Discussion started: 26 August 2026

References

Aldhaif, A. M., Stahl, C., Braun, R. A., Moghaddam, M. A., Shingler, T., Crosbie, E., Sawamura, P., Dadashazar, H., Ziemba, L., Jimenez, J. L., Campuzano-Jost, P., and Sorooshian, A.: Characterization of the Real Part of Dry Aerosol Refractive Index Over North America From the Surface to 12 Km, Journal of Geophysical Research: Atmospheres, 123, 8283–8300, https://doi.org/10.1029/2018JD028504, 2018.

Asher, E., Todt, M., Rosenlof, K., Thornberry, T., Gao, R.-S., Taha, G., Walter, P., Alvarez, S., Flynn, J., Davis, S. M., Evan, S., Brioude, J., Metzger, J.-M., Hurst, D. F., Hall, E., and Xiong, K.: Unexpectedly Rapid Aerosol Formation in the Hunga Tonga Plume, Proceedings of the National Academy of Sciences, 120, e2219547 120, https://doi.org/10.1073/pnas.2219547120, 2023.

Bigg, E. K., Ono, A., and Thompson, W. J.: Aerosols at Altitudes between 20 and 37 Km, Tellus XXII, 22, 550–563, https://doi.org/10.3402/tellusa.v22i5.10250, 1970.

Brodowsky, C. V., Sukhodolov, T., Chiodo, G., Aquila, V., Bekki, S., Dhomse, S. S., Höpfner, M., Laakso, A., Mann, G. W., Niemeier, U., Pitari, G., Quaglia, I., Rozanov, E., Schmidt, A., Sekiya, T., Tilmes, S., Timmreck, C., Vattioni, S., Visioni, D., Yu, P., Zhu, Y., and Peter, T.: Analysis of the Global Atmospheric Background Sulfur Budget in a Multi-Model Framework, Atmospheric Chemistry and Physics, 24, 5513–5548, https://doi.org/10.5194/acp-24-5513-2024, 2024.

Deshler, T. and Kalnajs, L. E.: Ratios of Extinction Coefficient, Mass, and Surface Area to Backscatter Coefficient and Mass to Extinction Coefficient Derived From Balloon-Borne Stratospheric Aerosol Size Distribution Measurements From 1989–2025, Journal of Geophysical Research: Atmospheres, 131, e2025JD045 262, https://doi.org/10.1029/2025JD045262, 2026.

Deshler, T., Anderson-Sprecher, R., Jäger, H., Barnes, J., Hofmann, D. J., Clemesha, B., Simonich, D., Osborn, M., Grainger, R. G., and Godin-Beekmann, S.: Trends in the Nonvolcanic Component of Stratospheric Aerosol over the Period 1971–2004, Journal of Geophysical Research: Atmospheres, 111, 2005JD006 089, https://doi.org/10.1029/2005JD006089, 2006.

Eckhardt, S., Prata, A. J., Seibert, P., Stebel, K., and Stohl, A.: Estimation of the Vertical Profile of Sulfur Dioxide Injection into the Atmosphere by a Volcanic Eruption Using Satellite Column Measurements and Inverse Transport Modeling, Atmos. Chem. Phys., 2008.

Gao, R. S., Telg, H., McLaughlin, R. J., Ciciora, S. J., Watts, L. A., Richardson, M. S., Schwarz, J. P., Perring, A. E., Thornberry, T. D., Rollins, A. W., Markovic, M. Z., Bates, T. S., Johnson, J. E., and Fahey, D. W.: A Light-Weight, High-Sensitivity Particle Spectrometer for PM2.5 Aerosol Measurements, Aerosol Science and Technology, 50, 88–99, https://doi.org/10.1080/02786826.2015.1131809, 2016.

Gurganus, C., Bednarz, E. M., Rollins, A., Waxman, E., Ray, E., Hintsa, E., Moore, F., Nance, D., Hall, B., Montzka, S. A., Vimont, I., Schwarz, J. P., DeLone, S., Ciciora, S., Abou-Rizk, S., Zhang, J., and Thornberry, T.: Constraining the Stratospheric Sulfate Budget in Global Models: Insights From In Situ OCS Measurements During 2023 SABRE and Comparison With Satellite, Balloon and Surface Data, Geophysical Research Letters, 53, e2025GL117 405, https://doi.org/10.1029/2025GL117405, 2026.

Hall, E. G., Jordan, A. F., Hurst, D. F., Oltmans, S. J., Vömel, H., Kühnreich, B., and Ebert, V.: Advancements, Measurement Uncertainties, and Recent Comparisons of the NOAAfrost Point Hygrometer, Atmospheric Measurement Techniques, 9, 4295–4310, https://doi.org/10.5194/amt-9-4295-2016, 2016.

Hazra, M. K., Ghoshal, S., Mahata, P., and Maiti, B.: Sulfuric Acid Decomposition Chemistry above Junge Layer in Earth's Atmosphere Concerning Ozone Depletion and Healing, Communications Chemistry, 2, 75, https://doi.org/10.1038/s42004-019-0178-4, 2019.

Hervig, M. and Deshler, T.: Evaluation of Aerosol Measurements from SAGE II, HALOE, and Balloonborne Optical Particle Counters, Journal of Geophysical Research: Atmospheres, 107, https://doi.org/10.1029/2001JD000703, 2002.

https://doi.org/10.5194/essd-2026-644
Preprint. Discussion started: 26 August 2026

Hofmann, D., Barnes, J., O'Neill, M., Trudeau, M., and Neely, R.: Increase in Background Stratospheric Aerosol Observed with Lidar at Mauna Loa Observatory and Boulder, Colorado, Geophysical Research Letters, 36, 2009GL039 008, https://doi.org/10.1029/2009GL039008, 2009.

Hooghiem, J. J. D., Popa, M. E., Röckmann, T., Grooß, J.-U., Tritscher, I., Müller, R., Kivi, R., and Chen, H.: Wildfire Smoke in the Lower Stratosphere Identified by in Situ CO Observations, Atmospheric Chemistry and Physics, 20, 13 985–14 003, https://doi.org/10.5194/acp-20-13985-2020, 2020.

Jäger, H. and Deshler, T.: Lidar Backscatter to Extinction, Mass and Area Conversions for Stratospheric Aerosols Based on Midlatitude Balloonborne Size Distribution Measurements, Geophysical Research Letters, 29, https://doi.org/10.1029/2002GL015609, 2002.

Junge, C. E. and Manson, J. E.: Stratospheric Aerosol Studies, Journal of Geophysical Research, 66, 2163–2182, https://doi.org/10.1029/JZ066i007p02163, 1961.

Junge, C. E., Chagnon, C. W., and Manson, J. E.: Stratospheric Aerosols, Journal of Meteorology, 18, 81–108, https://doi.org/10.1175/1520-0469(1961)018<0081:SA>2.0.CO;2, 1961.

Kalnajs, L. E. and Deshler, T.: A New Instrument for Balloon-Borne *In Situ* Aerosol Size Distribution Measurements, the Continuation of a 50 Year Record of Stratospheric Aerosols Measurements, Journal of Geophysical Research: Atmospheres, 127, e2022JD037 485, https://doi.org/10.1029/2022JD037485, 2022.

Khaykin, S. M., Godin-Beekmann, S., Keckhut, P., Hauchecorne, A., Jumelet, J., Vernier, J.-P., Bourassa, A., Degenstein, D. A., Rieger, L. A., Bingen, C., Vanhellemont, F., Robert, C., DeLand, M., and Bhartia, P. K.: Variability and Evolution of the Midlatitude Stratospheric Aerosol Budget from 22 Years of Ground-Based Lidar and Satellite Observations, Atmospheric Chemistry and Physics, 17, 1829–1845, https://doi.org/10.5194/acp-17-1829-2017, 2017.

Lawler, M. J., Schill, G. P., Murphy, D. M., Abou-Ghanem, M., Brock, C. A., Lyu, M., Ahern, A. T., Taylor, S. J., Hintsa, E. J., Moore, F. L., Dutton, G. S., Nance, J. D., Hall, B. D., Pierce, R. B., Ray, E. A., and Thornberry, T. D.: The Composition and Stratospheric Fate of Aerosol Particles Originating in the Polar Vortex, Journal of Geophysical Research: Atmospheres, 130, e2025JD043 530, https://doi.org/10.1029/2025JD043530, 2025.

Li, D., Vogel, B., Wang, L., Bai, Z., Qie, K., Peng, D., Xu, J., Li, Q., Yang, Z., Han, T., Wang, S., Xu, X., and Bian, J.: In-Situ Measurements of Dust Aerosols Transported Into the Lower Stratosphere From a Dust Storm Event, Geophysical Research Letters, 52, e2025GL117 342, https://doi.org/10.1029/2025GL117342, 2025.

Li, Y., Dykema, J., Deshler, T., and Keutsch, F.: Composition Dependence of Stratospheric Aerosol Shortwave Radiative Forcing in Northern Midlatitudes, Geophysical Research Letters, 48, e2021GL094 427, https://doi.org/10.1029/2021GL094427, 2021.

Li, Y., Bai, B., Dykema, J., Shin, N., Lambe, A. T., Chen, Q., Kuwata, M., Ng, N. L., Keutsch, F. N., and Liu, P.: Predicting Real Refractive Index of Organic Aerosols From Elemental Composition, Geophysical Research Letters, 50, e2023GL103 446, https://doi.org/10.1029/2023GL103446, 2023.

Lyu, M., Ahern, A. T., Schill, G. P., Lawler, M. J., Murphy, D. M., Taylor, S. J., Fodel, A., Abou-Ghanem, M., Gurganus, C., Zhu, Y., Tilmes, S., Ray, E., Thornberry, T. D., Gao, R.-S., Hintsa, E. J., Moore, F., Dutton, G., Nance, D., Hall, B., Rollins, A. W., Waxman, E. M., Zuraski, K., Diskin, G. S., Choi, Y., Pierce, R. B., Weinzierl, B., Kuderna, F., Dollner, M., Jensen, E., and Brock, C. A.: An Unrecognized Mode of Small Particles in the Lower Stratosphere, Science, 392, eadw8939, https://doi.org/10.1126/science.adw8939, 2026.

Martinsson, B. G., Friberg, J., Sandvik, O. S., Hermann, M., Van Velthoven, P. F. J., and Zahn, A.: Formation and Composition of the UTLS Aerosol, npj Climate and Atmospheric Science, 2, 40, https://doi.org/10.1038/s41612-019-0097-1, 2019.

https://doi.org/10.5194/essd-2026-644
Preprint. Discussion started: 26 August 2026

McCormick, M. P., Thomason, L. W., and Trepte, C. R.: Atmospheric Effects of the Mt Pinatubo Eruption, Nature, 373, 399–404, https://doi.org/10.1038/373399a0, 1995.

Minnis, P., Harrison, E. F., Stowe, L. L., Gibson, G. G., Denn, F. M., Doelling, D. R., and Smith, W. L.: Radiative Climate Forcing by the Mount Pinatubo Eruption, Science, 259, 1411–1415, https://doi.org/10.1126/science.259.5100.1411, 1993.

Murphy, D. M.: Effect of Stratospheric Aerosols on Direct Sunlight and Implications for Concentrating Solar Power, Environmental Science & Technology, 43, 2784–2786, https://doi.org/10.1021/es802206b, 2009.

Murphy, D. M., Froyd, K. D., Bourgeois, I., Brock, C. A., Kupc, A., Peischl, J., Schill, G. P., Thompson, C. R., Williamson, C. J., and Yu, P.: Radiative and Chemical Implications of the Size and Composition of Aerosol Particles in the Existing or Modified Global Stratosphere, Atmospheric Chemistry and Physics, 21, 8915–8932, https://doi.org/10.5194/acp-21-8915-2021, 2021.

Ohneiser, K., Ansmann, A., Kaifler, B., Chudnovsky, A., Barja, B., Knopf, D. A., Kaifler, N., Baars, H., Seifert, P., Villanueva, D., Jimenez, C., Radenz, M., Engelmann, R., Veselovskii, I., and Zamorano, F.: Australian Wildfire Smoke in the Stratosphere: The Decay Phase in 2020/2021 and Impact on Ozone Depletion, Atmospheric Chemistry and Physics, 22, 7417–7442, https://doi.org/10.5194/acp-22-7417-2022, 2022.

Pan, L. L., Atlas, E. L., Salawitch, R. J., Honomichl, S. B., Bresch, J. F., Randel, W. J., Apel, E. C., Hornbrook, R. S., Weinheimer, A. J., Anderson, D. C., Andrews, S. J., Baidar, S., Beaton, S. P., Campos, T. L., Carpenter, L. J., Chen, D., Dix, B., Donets, V., Hall, S. R., Hanisco, T. F., Homeyer, C. R., Huey, L. G., Jensen, J. B., Kaser, L., Kinnison, D. E., Koenig, T. K., Lamarque, J.-F., Liu, C., Luo, J., Luo, Z. J., Montzka, D. D., Nicely, J. M., Pierce, R. B., Riemer, D. D., Robinson, T., Romashkin, P., Saiz-Lopez, A., Schauffler, S., Shieh, O., Stell, M. H., Ullmann, K., Vaughan, G., Volkamer, R., and Wolfe, G.: The Convective Transport of Active Species in the Tropics (CONTRAST) Experiment, Bulletin of the American Meteorological Society, 98, 106–128, https://doi.org/10.1175/BAMS-D-14-00272.1, 2017.

Regayre, L. A., Prévost, L. M. C., Ghosh, K., Johnson, J. S., Oakley, J. E., Owen, J., Webb, I., and Carslaw, K. S.: Remaining Aerosol Forcing Uncertainty after Observational Constraint and the Processes That Cause It, Atmospheric Chemistry and Physics, 26, 2293–2317, https://doi.org/10.5194/acp-26-2293-2026, 2026.

Robock, A.: Volcanic Eruptions and Climate, Reviews of Geophysics, 38, 191–219, https://doi.org/10.1029/1998RG000054, 2000.

Shin, J., Sim, J., Kim, D., and Noh, Y.: Simple Retrieval of the Real Part of the Refractive Index for Ambient Aerosols Using Extinction Coefficient Analysis via Camera and Volume Size Distribution, Atmospheric Environment, 330, 120 537, https://doi.org/10.1016/j.atmosenv.2024.120537, 2024.

Smith, K., Baron, A., Thornberry, T., Schwarz, J., Asher, E., Hall, E., Cullis, P., Fritz, A., Telg, H., Burgener, R., Thomas, B., Martinsen, M., Nardini, D., Kuniyaki, D., Smale, P., Liley, B., Querel, R., Kopka, K., Crocker, R. I., Jordan, S., Doneghey, M., Longren, L., Evan, S., Brioude, J., Metzger, J.-M., Combemale, D., Becker, C., Samuel, D., Tjon A Ten, C., Amierali, M., Wongsowidjojo, C., Rodrigues, D., Paiman, G., Piters, A., and Mueller, K.: Aerosol number and size distribution data (140 - 2500 nm) from the Balloon Baseline Stratospheric Aerosol Profiles (B2SAP) network, https://doi.org/10.25921/mchy-y552, 2026.

Solomon, S., Garciat, R. R., Rowland, F. S., and Wuebbles, D. J.: On the Depletion of Antarctic Ozone, Nature, 321, 755–758, 1986.

Solomon, S., Daniel, J. S., Neely, R. R., Vernier, J.-P., Dutton, E. G., and Thomason, L. W.: The Persistently Variable "Background" Stratospheric Aerosol Layer and Global Climate Change, Science, 333, 866–870, https://doi.org/10.1126/science.1206027, 2011.

Solomon, S., Stone, K., Yu, P., Murphy, D. M., Kinnison, D., Ravishankara, A. R., and Wang, P.: Chlorine Activation and Enhanced Ozone Depletion Induced by Wildfire Aerosol, Nature, 615, 259–264, https://doi.org/10.1038/s41586-022-05683-0, 2023.

https://doi.org/10.5194/essd-2026-644
Preprint. Discussion started: 26 August 2026

Stenchikov, G., Hamilton, K., Stouffer, R. J., Robock, A., Ramaswamy, V., Santer, B., and Graf, H.-F.: Arctic Oscillation Response to Volcanic Eruptions in the IPCC AR4 Climate Models, Journal of Geophysical Research: Atmospheres, 111, 2005JD006 286, https://doi.org/10.1029/2005JD006286, 2006.

Sterling, C. W., Johnson, B. J., Oltmans, S. J., Smit, H. G. J., Jordan, A. F., Cullis, P. D., Hall, E. G., Thompson, A. M., and Witte, J. C.: Homogenizing and Estimating the Uncertainty in NOAA's Long-Term Vertical Ozone Profile Records Measured with the Electrochemical Concentration Cell Ozonesonde, Atmospheric Measurement Techniques, 11, 3661–3687, https://doi.org/10.5194/amt-11-3661-2018, 2018.

Sumlin, B. J., Heinson, W. R., and Chakrabarty, R. K.: Retrieving the Aerosol Complex Refractive Index Using PyMieScatt: A Mie Computational Package with Visualization Capabilities, Journal of Quantitative Spectroscopy and Radiative Transfer, 205, 127–134, https://doi.org/10.1016/j.jqsrt.2017.10.012, 2018.

Thomason, L. W. and Burton, S. P.: SAGE II Measurements of Stratospheric Aerosol Properties at Non-Volcanic Levels, Atmos. Chem. Phys., 2008.

Todt, M. A., Asher, E., Hall, E., Cullis, P., Jordan, A., Xiong, K., Hurst, D. F., and Thornberry, T.: Baseline Balloon Stratospheric Aerosol Profiles (B^2 SAP)—Systematic Measurements of Aerosol Number Density and Size, Journal of Geophysical Research: Atmospheres, 128, e2022JD038 041, https://doi.org/10.1029/2022JD038041, 2023.

Trickl, T., Giehl, H., Jäger, H., and Vogelmann, H.: 35 Yr of Stratospheric Aerosol Measurements at Garmisch-Partenkirchen: From Fuego to Eyjafjallajökull, and Beyond, Atmospheric Chemistry and Physics, 13, 5205–5225, https://doi.org/10.5194/acp-13-5205-2013, 2013.

Turco, R. P., Whitten, R. C., and Toon, O. B.: Stratospheric Aerosols: Observation and Theory, Reviews of Geophysics, 20, 233–279, https://doi.org/10.1029/RG020i002p00233, 1982.

Ueyama, R., Smith, W. P., Brown, M., Jensen, E. J., Ziemba, L., Bui, T. P., Dean-Day, J., and Williamson, C. J.: On the Fate of Aerosols Produced by New Particle Formation in the Upper Troposphere and Lower Stratosphere, Geophysical Research Letters, 52, e2025GL116 860, https://doi.org/10.1029/2025GL116860, 2025.

Vernier, J.-P., Thomason, L. W., Pommereau, J.-P., Bourassa, A., Pelon, J., Garnier, A., Hauchecorne, A., Blanot, L., Trepte, C., Degenstein, D., and Vargas, F.: Major Influence of Tropical Volcanic Eruptions on the Stratospheric Aerosol Layer during the Last Decade: VOLCANIC INFLUENCE AERO STRATO, Geophysical Research Letters, 38, n/a–n/a, https://doi.org/10.1029/2011GL047563, 2011.

Von Savigny, C. and Hoffmann, C. G.: Issues Related to the Retrieval of Stratospheric-Aerosol Particle Size Information Based on Optical Measurements, Atmospheric Measurement Techniques, 13, 1909–1920, https://doi.org/10.5194/amt-13-1909-2020, 2020.

Wegner, T., Grooß, J.-U., Von Hobe, M., Stroh, F., Sumińska-Ebersoldt, O., Volk, C. M., Hösen, E., Mitev, V., Shur, G., and Müller, R.: Heterogeneous Chlorine Activation on Stratospheric Aerosols and Clouds in the Arctic Polar Vortex, Atmospheric Chemistry and Physics, 12, 11 095–11 106, https://doi.org/10.5194/acp-12-11095-2012, 2012.

Womack, C. C., Manfred, K. M., Wagner, N. L., Adler, G., Franchin, A., Lamb, K. D., Middlebrook, A. M., Schwarz, J. P., Brock, C. A., Brown, S. S., and Washenfelder, R. A.: Complex Refractive Indices in the Ultraviolet and Visible Spectral Region for Highly Absorbing Non-Spherical Biomass Burning Aerosol, Atmospheric Chemistry and Physics, 21, 7235–7252, https://doi.org/10.5194/acp-21-7235-2021, 2021.

Wrana, F., Von Savigny, C., Zalach, J., and Thomason, L. W.: Retrieval of Stratospheric Aerosol Size Distribution Parameters Using Satellite Solar Occultation Measurements at Three Wavelengths, Atmospheric Measurement Techniques, 14, 2345–2357, https://doi.org/10.5194/amt-14-2345-2021, 2021.

https://doi.org/10.5194/essd-2026-644
Preprint. Discussion started: 26 August 2026

Zhu, Y., Yu, P., Wang, X., Bardeen, C., Borrmann, S., Höpfner, M., Mahnke, C., Weigel, R., Krämer, M., Deshler, T., Bian, J., Bai, Z., Vernier, H., Portmann, R. W., Rosenlof, K. H., Kloss, C., Pan, L. L., Smith, W., Honomichl, S., Zhang, J., Stone, K. A., and Toon, O. B.: Evaluating the Importance of Nitrate-Containing Aerosols for the Asian Tropopause Aerosol Layer, Journal of Geophysical Research: Atmospheres, 129, e2024JD041 283, https://doi.org/10.1029/2024JD041283, 2024.